Effect of external mean flow on sound transmission loss of double-walled porous functionally graded magneto-electro-elastic sandwich plates

Sayan Sirimontree
Thammasat University
Chanachai Thongchom
Thammasat University
Peyman Roodgar Saffari
Thammasat University
Pouyan Roodgar Saffari
Thammasat University
Nima Refahati (refahati@damavandiau.ac.ir)
Islamic Azad University of Damavand
Thira Jearsiripongkul
Thammasat University
Suraparb Keawsawasvong
Thammasat University

Article

Keywords: Sound Transmission Loss, Magneto-electro-elastic Plate, Porosity, Functionally Graded Material, Third-Order Shear Deformation Theory

Posted Date: May 27th, 2022

DOI: https://doi.org/10.21203/rs.3.rs-1674531/v1

Effect of external mean flow on sound transmission loss of double-walled porous functionally graded magneto-electro-elastic sandwich plates

Sayan Sirimontree[1], Chanachai Thongchom[1*], Peyman Roodgar Saffari[1*], Pouyan Roodgar Saffari[1], Nima Refahati

[2*], Thira Jearsiripongkul[3], Suraparb Keawsawasvong[1]

[1]Department of Civil Engineering, Faculty of Engineering, Thammasat School of Engineering, Thammasat University, Pathumthani 12120, Thailand
[2]Department of Mechanical Engineering, Damavand Branch, Islamic Azad University, Damavand P.O. Box 3971878911, Iran
[3]Department of Mechanical Engineering, Faculty of Engineering, Thammasat School of Engineering, Thammasat University, Pathumthani 12120, Thailand

. **Corresponding author:*

. *Chanachai Thongchom(Tchanach@engr.tu.ac.th)*

. *Peyman Roodgar saffari (peyman.saffari1364@gmail.com, rpeyman@engr.tu.ac.th)*

. *Nima Refahati (refahati@damavandiau.ac.ir, nima.refahati1978@gmail.com)*

Abstract

In the present study, the sound transmission loss through the air-filled rectangular double-walled sandwich smart magneto-electro-elastic (MEE) plates with porous functionally graded material (PFGM) core layer under initial external electric and magnetic potentials, and external mean airflow is studied using the third-order shear deformation theory (TSDT). Three states of uneven porosity distributions are considered for PFGM core layer which are supposed to vary along the in-plane and thickness directions based on the power-law model. The derivation of vibroacoustic equations in the form of coupled relations is realized by implementing Hamilton's principle. An analytical approach, i.e. second velocity potential, is exploited to solve them in conjunction with double Fourier series, and the final result is the desired sound transmission loss (STL) equation. The developed solution is investigated in terms of its accuracy and precision via a comparison with other available data in existing research. Parameter studies reveal the impacts of the initial electric and magnetic potentials, porosity distributions, incident angles, acoustic cavity depth on STL through the double-walled sandwich smart MEE plates.

Keywords Sound Transmission Loss, Magneto-electro-elastic Plate, Porosity, Functionally Graded Material, Third-Order Shear Deformation Theory.

I. Introduction

Introducing the concept of porosity in other fields of sciences has resulted in interesting concepts such as metal foams that present various advantages such as superior energy absorption [1] and resistance to heat and impact [2]. The shape of the pores, pore strut or wall arrangement, surface area and surface roughness, in addition to porosity and pore size, determine the behavior of porous materials. It is, thus, mandatory to define the relation between pore features and physical behavior of such materials to be able to use them in different applications or studies. Until now, several experimental and numerical projects investigated the influence of the porous materials on

the dynamic problems, such as, free and forced vibration of beams [3], plates [4], and cylindrical shells [5]. Because of high stiffness-to-weight rations and high strength to-weight in plates, these significant structural components are applied in many engineering applications like aviation, buildings, submarines, and automotive [6–9]. Al Rjoub and Alshatnawi [10] investigated the influence of even porosity distribution on the variations of natural frequencies of functionally-graded material (FGM) cracked plate using The power law model. Formed from a combination of metal and ceramic, FGMs display a uniformly-varying distribution of properties along a desired path in the structure. Muc and Flis [11] studied the flutter characteristics and free vibrations of PFGM plates via the TSDT, analytical and Rayleigh-Ritz methods. Roodgar Saffari et al. [12–15] used NSGT in the framework of the first-order shear deformation shell assumption to study the free vibration of fluid-conveying BN nanotubes. Hashemi et al. [16] used Poincare–Lindstedt method (MPLM) to analyze the nonlinear free vibration behavior of in-plane bi-directional PFGM plate. Quan et al. [17,18] indicated the effect of the porosity coefficient, volume fraction index, and elastic medium on the nonlinear vibration of PFGM sandwich plate subjected to the blast loading. Thongchom et al. [19, 21] investigated tensile strength and modulus of elasticity nanocomposite and sound transmission loss of sandwich cylindrical shell

The capability of smart materials including piezoelectric (PZT), MEE, electrorheological fluid (ERF) to adept their properties in reaction to environmental factors including electricity, magnetic, heat, and loading is one of the major reasons for the wide range of studies conducted on them [22,23]. MEE composites constitute a motivating type of composite smart materials which offer the advantages of both piezomagnetism and piezoelectricity. The ability provided by converting energy between different phases partly explains the interest of researchers into these materials [24–26]. Vinyas and Kattimani [27] presented a finite element method (FEM) to calculate the static parameters of FG MEE rectangular plates under the thermal environment. A simple velocity feedback control law for vibration suppression skew MEE plates utilizing active constrained layer damping (ACLD) based on the layerwise shear deformation theory was carried out by Vinyas [28]. Also, Vinyas [29] numerically analyzed the effect of porous properties on the frequency response of FGM MEE circular and annular plates taking account the third-order shear deformation theory TSDT and the FEM. Ebrahimi et al. [30] studied the effects of magnetic and electric potentials in conjunction with porosity volume fraction on the variations of FGM-MEE plate resting on elastic substrate applying TSDT. Arshid et al. [31] used the generalized differential quadrature method (GDQM) to investigate the natural frequencies of annular plate made up of FGM MEE under multi physical loads. Hamidi et al. [32] presented the dynamic behavior of MEE multilayer plates on the elastic substrate. Esayas and Kattimani [33] analyzed the influences of the porosity on the nonlinear vibration of FGM-MEE plates constricted layer damping patches. Sh et al. [34] used FSDT and finite element method (FEM) to study the geometrically nonlinear free vibration and transient problem of porous FGM-MEE plates. Dat et al. [35] investigated the effect of temperature increment, magnetic and electric potentials on the vibration behavior of sandwich MEE plate under blast loading.

The study on double-walled structures is inseparable from the research on double-walled plates as they are promising components in rapid transit, aerospace vehicles and double-glazed windows, among others [36]. Outstanding features of double-walled structures in mechanical and acoustic aspects have made them an attractive choice in different fields of science from civil engineering to aerospace [37–39]. The continuous research on their noise cancellation characteristics is one important area where their great potential is being exploited via empirical and analytical means. The literature is rich in studies focusing on the vibroacoustic features of noise transmission of single or double-walled shells and plates. A statistical energy analysis (SEA) was presented by Oliazadeh et al. [40] to estimate sound transmission loss (STL) through single-and double-walled thin rectangular plates considering absorbing material. A common method of evaluation of noise attenuation is the measurement of sound transmission loss. To this aim, the energy of the impingent sound waves is divided over that of the transmitted sound waves. The resulting ratio is usually expressed in dB. They validated their results with the experimental outcomes and demonstrated that filling the acoustic cavity between the double-walled plate with lightweight absorbing material like fiberglass rises the STL at the critical frequency. Xin et al. [41] studied the influence of external mean flow on the changes of STL of double rectangular plate via acoustic velocity potential. The STL through the triple-panel partition is compared with that of a double-panel partition by Xin and Lu [42] for clamped boundary conditions. Talebitooti et al. [43] employed wo-variable refined plate theory for predicting the STL cross laminated composite plate in the presence of external mean flow. Based on the viscoelastic Zener model in the framework of FSDT, Amirinezhad et al. [44] analyzed the wave propagation across plate made of polymeric foam. The main results denoted that increasing damping reduces the stiffness and therefore reduces STL in high frequencies. Danesh and Ghadami [45] analytically investigated the effect of electric voltage of piezoelectric materials on the variation of STL through double-walled FGM piezoelectric plate using TSDT. They proved that Using Helium and Hydrogen gases for filling the acoustic cavity between the two piezoelectric plates has a substantial effect on the sound isolation performance. Recently, Hasheminejad and Jamalpoor [46] applied the classical plate theory (CPT) and multi-input multi-output sliding mode control (MIMOSMC) plan to improve the STL of simply supported hybrid smart double sandwich plate including PZT and ERF materials. The enhancement of STL through a double-plate structure around the mass-air-mass resonance frequency is presented by Mao [47] using electromagnetic shunt damper (EMSD). Wang et al. [48] analyzed the effect of the external mean flow on the STL of a metamaterial plate submerged in moving fluids. Based on the TSDT and Rayleigh integral, Gunasekaran et al. [49] investigated the vibroacoustic behavior of FGM graphene reinforced composite plate subjected to the nonuniform edge loads. Ghassabi and Talebitooti [50] applied three-dimensional (3D) theory of elasticity to study the acoustic response of MEE shell structure.

Despite the growing attention to different aspects of single or double-walled plates with respect to their noise transmission, the authors found no relevant study on the STL of a finite double-walled simply supported sandwich PFGM-MEE plate under the action of harmonic plane sound waves in the presence of external mean flow based on the assumptions of TSDT. The current

research tries to cover this gap and provide insightful explanations on the behavior of such structures. The material characteristics of PFGM core layer change slowly through the thickness via power-law scheme. Using Hamilton's principle and TSDT, the coupled vibroacoustic equations are derived. One of the methods to solve the derived vibroacoustic equations is the sound velocity potential approach. This method is employed here to solve the coupled equations of the considered double-walled plate with the equations of acoustic cavity included.

2. Preliminary formulations

The problem schematic is displayed in Fig. 1. One should note the employed Cartesian coordinates defined for the double-walled rectangular sandwich MEE ($a \times b$) plate encompassing the acoustic cavity baffled in a wall of infinite dimensions. Also, a plane sound wave of time-harmonic nature, with the azimuth angle $0^{\circ} \leq \alpha \leq 360^{\circ}$ and elevation angle $0^{\circ} \leq \beta \leq 90^{\circ}$, impinges the top surface of upper MEE plate. It is supposed that each sandwich MEE plate is composed of two identical BaTiO3-CoFe2O4 piezomagnetic layers with uniform thickness h_{m} and PFGM core layer with uniform thickness h_{c}. Furthermore, each MEE plate is subjected to electric $\Upsilon(x, y, z, t)$ and magnetic $\psi(x, y, z, t)$ potentials. As can be seen, the acoustic cavity depth is denoted with the symbol L. As can be seen, an external mean flow passes in the incident field with a constant velocity V.

2.1. Constitutive relations

To derive the dynamic equations governing the motion, based on the TSDT which considers both rotary inertia and shear deformation in the transverse direction, the classical displacement field (U, V, W) in Cartesian coordinates for each sandwich MEE plate is employed in the form [51]

$$
\begin{aligned}
U_i(x, y, z, t) &= u_{0i}(x, y, t) + z\theta_{xi}(x, y, t) - \frac{4z^3}{3h^2}\left(\theta_{xi}(x, y, t) + \frac{\partial W_{0i}(x,y,t)}{\partial x}\right), \\
V_i(x, y, z, t) &= v_{0i}(x, y, t) + z\theta_{yi}(x, y, t) - \frac{4z^3}{3h^2}\left(\theta_{yi}(x, y, t) + \frac{\partial W_{0i}(x,y,t)}{\partial y}\right), \\
W_i(x, y, z, t) &= W_{0i}(x, y, t),
\end{aligned}
\tag{1}
$$

where $i = 1,2$, in plane deflections of the mid-surface along x and y directions presented with u_0 and v_0, respectively. Furthermore θ_y and θ_x are the rotations of the middle plane along x and y directions, respectively, and w denotes the lateral plate displacement. Regarding the linear strain-displacement relation, the normal $(\varepsilon_{xx}, \varepsilon_{yy})$ and shear $(\gamma_{xz}, \gamma_{yz}, \gamma_{xy})$ strain components of each sandwich MEE plate are defined as

$$\varepsilon_{xxi} = \frac{\partial u_{0i}}{\partial x} + z\frac{\partial \theta_{xi}}{\partial x} - C_1 z^3\left(\frac{\partial \theta_{xi}}{\partial x} + \frac{\partial^2 W_{0i}}{\partial x^2}\right),$$
$$\varepsilon_{yyi} = \frac{\partial v_{0i}}{\partial y} + z\frac{\partial \theta_{y}}{\partial y} - C_1 z^3\left(\frac{\partial \theta_{y}}{\partial y} + \frac{\partial^2 W_{0i}}{\partial y^2}\right), \tag{2}$$
$$\gamma_{xyi} = \frac{\partial u_{0i}}{\partial y} + \frac{\partial v_{0i}}{\partial x} + z\left(\frac{\partial \theta_{xi}}{\partial y} + \frac{\partial \theta_{yi}}{\partial x}\right) - C_1 z^3\left(\frac{\partial \theta_{xi}}{\partial y} + \frac{\partial \theta_{yi}}{\partial x} + 2\frac{\partial^2 W_{0i}}{\partial x \partial y}\right),$$
$$\gamma_{xzi} = (1 - 3C_1 z^2)\left(\theta_{xi} + \frac{\partial W_{0i}}{\partial x}\right),$$
$$\gamma_{yz} = (1 - 3C_1 z^2)\left(\theta_{yi} + \frac{\partial W_{0i}}{\partial y}\right)$$

where $i = 1,2$ and $C_1 = \frac{4}{3h^2}$. The classical constitutive stress-strain relations including normal $(\sigma_{xx}, \sigma_{yy})$ and shear $(\tau_{xz}, \tau_{yz}, \tau_{xy})$ stress components for the PFGM core layer in each sandwich plate are presented as

$$\begin{Bmatrix} \sigma_{xxi} \\ \sigma_{yyi} \\ \tau_{yzi} \\ \tau_{xzi} \\ \tau_{xyi} \end{Bmatrix}_{\text{PFGM}} = \begin{bmatrix} Q_{11}(z) & Q_{12(z)} & 0 & 0 & 0 \\ Q_{12(z)} & Q_{22}(z) & 0 & 0 & 0 \\ 0 & 0 & Q_{66}(z) & 0 & 0 \\ 0 & 0 & 0 & Q_{44}(z) & 0 \\ 0 & 0 & 0 & 0 & Q_{55}(z) \end{bmatrix}_{\text{PFGM}} \begin{Bmatrix} \varepsilon_{xxi} \\ \varepsilon_{yyi} \\ \gamma_{yzi} \\ \gamma_{xzi} \\ \gamma_{xyi} \end{Bmatrix}, \tag{3}$$

$$Q_{11} = \frac{E(z)}{1-\vartheta^2(z)}, Q_{22} = \frac{E(z)}{1-\vartheta^2(z)}, Q_{12} = \frac{\vartheta(z)E(z)}{1-\vartheta^2(z)}, Q_{66} = G_{12}(z), Q_{44} = G_{23}(z), Q_{55} = G_{13}(z).$$

where $i = 1,2$. E and ϑ refer to Young modulus and Poisson's ratio, respectively. To achieve FG-like properties, the bottom and top surfaces of the core layer are purely made from metal and ceramic, respectively. As already described, three porosity distribution patterns are considered for this study. Accordingly, the corresponding values of elastic modulus, mass density and Poisson's ratio based on the rule of mixture with three different types of uneven porosity distributions are described as [52]

Type A:

$$E(z) = (E_{\text{c}} - E_{\text{m}})(z/h + 0.5)^p + E_{\text{m}} - \left(1 - e^{-0.5\zeta}\right)(E_{\text{c}} + E_{\text{m}})(1 - 2\,|z|/h_{\text{c}}),$$
$$\rho(z) = (\rho_{\text{c}} - \rho_{\text{m}})(z/h + 0.5)^p + \rho_{\text{m}} - \left(1 - e^{-0.5\zeta}\right)(\rho_{\text{c}} + \rho_{\text{m}})(1 - 2\,|z|/h_{\text{c}}), \tag{4}$$
$$\vartheta(z) = (\vartheta_{\text{c}} - \vartheta_{\text{m}})(z/h + 0.5)^p + \vartheta_{\text{m}} - \left(1 - e^{-0.5\zeta}\right)(\vartheta_{\text{c}} + \vartheta_{\text{m}})(1 - 2\,|z|/h_{\text{c}}),$$

Type B:

$$E(z) = (E_{\text{c}} - E_{\text{m}})(z/h + 0.5)^p + E_{\text{m}} - \log(1 + 0.5\zeta)(E_{\text{c}} + E_{\text{m}})(1 - 2\,|z|/h),$$

$$\rho(z) = (\rho_{\mathrm{c}} - \rho_{\mathrm{m}})(z/h + 0.5)^p + \rho_{\mathrm{m}} - \log(1 + 0.5\zeta)(\rho_{\mathrm{c}} + \rho_{\mathrm{m}})(1 - 2\,|z|/h), \tag{5}$$

$$\vartheta(z) = (\vartheta_{\mathrm{c}} - \vartheta_{\mathrm{m}})(z/h + 0.5)^p + \vartheta_{\mathrm{m}} - \log(1 + 0.5\zeta)(\vartheta_{\mathrm{c}} + \vartheta_{\mathrm{m}})(1 - 2\,|z|/h)$$

Type C:

$$E(z) = (E_{\mathrm{c}} - E_{\mathrm{m}})(z/h + 0.5)^p + E_{\mathrm{m}} - 0.5\zeta(E_{\mathrm{c}} + E_{\mathrm{m}}),$$

$$\rho(z) = (\rho_{\mathrm{c}} - \rho_{\mathrm{m}})(z/h + 0.5)^p + \rho_{\mathrm{m}} - 0.5\zeta(\rho_{\mathrm{c}} + \rho_{\mathrm{m}}), \tag{6}$$

$$\vartheta(z) = (\vartheta_{\mathrm{c}} - \vartheta_{\mathrm{m}})(z/h + 0.5)^p + \vartheta_{\mathrm{m}} - 0.5\zeta(\vartheta_{\mathrm{c}} + \vartheta_{\mathrm{m}}),$$

in which m and c signify, respectively, metal and ceramic phases. Also, ρ is the mass density. The always-positive gradient index (p) is used in this study to determine the changes of a specific property in the thickness direction. The greater the gradient index, the more metallic the structure. Furthermore, ζ expresses the porosity coefficient. It is noteworthy that for each MEE plate, the basic relations including electric displacement and magnetic induction, and stress tensor can be expressed as [53]

$$\begin{Bmatrix} \sigma_{xxi} \\ \sigma_{yyi} \\ \tau_{yzi} \\ \tau_{xzi} \\ \tau_{xyi} \end{Bmatrix}_{\mathrm{m}} = \begin{bmatrix} c_{11} & c_{12} & 0 & 0 & 0 \\ c_{12} & c_{22} & 0 & 0 & 0 \\ 0 & 0 & c_{44} & 0 & 0 \\ 0 & 0 & 0 & c_{55} & 0 \\ 0 & 0 & 0 & 0 & c_{66} \end{bmatrix} \begin{Bmatrix} \varepsilon_{xxi} \\ \varepsilon_{yyi} \\ \gamma_{yzi} \\ \gamma_{xzi} \\ \gamma_{xyi} \end{Bmatrix} - \begin{bmatrix} 0 & 0 & e_{31} \\ 0 & 0 & e_{32} \\ 0 & e_{24} & 0 \\ e_{15} & 0 & 0 \\ 0 & 0 & 0 \end{bmatrix} \begin{Bmatrix} \mathrm{E}_{xi} \\ \mathrm{E}_{yi} \\ \mathrm{E}_{zi} \end{Bmatrix} -$$

$$\begin{bmatrix} 0 & 0 & f_{31} \\ 0 & 0 & f_{32} \\ 0 & f_{24} & 0 \\ f_{15} & 0 & 0 \\ 0 & 0 & 0 \end{bmatrix} \begin{Bmatrix} \mathcal{H}_{xi} \\ \mathcal{H}_{yi} \\ \mathcal{H}_{zi} \end{Bmatrix},$$

$$\begin{Bmatrix} D_{xi} \\ D_{yi} \\ D_{zi} \end{Bmatrix} = \begin{bmatrix} 0 & 0 & e_{31} \\ 0 & 0 & e_{32} \\ 0 & e_{24} & 0 \\ e_{15} & 0 & 0 \\ 0 & 0 & 0 \end{bmatrix}^T \begin{Bmatrix} \varepsilon_{xxi} \\ \varepsilon_{yyi} \\ \gamma_{yzi} \\ \gamma_{xzi} \\ \gamma_{xyi} \end{Bmatrix} + \begin{bmatrix} \kappa_{11} & 0 & 0 \\ 0 & \kappa_{22} & 0 \\ 0 & 0 & \kappa_{33} \end{bmatrix} \begin{Bmatrix} \mathrm{E}_{xi} \\ \mathrm{E}_{yi} \\ \mathrm{E}_{zi} \end{Bmatrix} + \begin{bmatrix} \mu_{11} & 0 & 0 \\ 0 & \mu_{22} & 0 \\ 0 & 0 & \mu_{33} \end{bmatrix} \begin{Bmatrix} \mathcal{H}_{xi} \\ \mathcal{H}_{yi} \\ \mathcal{H}_{zi} \end{Bmatrix}, \tag{7}$$

$$\begin{Bmatrix} B_{xi} \\ B_{yi} \\ B_{zi} \end{Bmatrix} = \begin{bmatrix} 0 & 0 & f_{31} \\ 0 & 0 & f_{32} \\ 0 & f_{24} & 0 \\ f_{15} & 0 & 0 \\ 0 & 0 & 0 \end{bmatrix}^T \begin{Bmatrix} \varepsilon_{xxi} \\ \varepsilon_{yyi} \\ \gamma_{yzi} \\ \gamma_{xzi} \\ \gamma_{xyi} \end{Bmatrix} + \begin{bmatrix} \mu_{11} & 0 & 0 \\ 0 & \mu_{22} & 0 \\ 0 & 0 & \mu_{33} \end{bmatrix} \begin{Bmatrix} \mathrm{E}_{xi} \\ \mathrm{E}_{yi} \\ \mathrm{E}_{zi} \end{Bmatrix} + \begin{bmatrix} \gamma_{11} & 0 & 0 \\ 0 & \gamma_{22} & 0 \\ 0 & 0 & \gamma_{33} \end{bmatrix} \begin{Bmatrix} \mathcal{H}_{xi} \\ \mathcal{H}_{yi} \\ \mathcal{H}_{zi} \end{Bmatrix},$$

where $i = 1,2$. Furthermore, $[\mathbf{B}]$ and $[\mathbf{D}]$ indicate the magnetic induction and electric displacement, respectively. Furthermore, $[\boldsymbol{\gamma}], [\boldsymbol{\mu}], [\boldsymbol{\kappa}], [\boldsymbol{f}], [\boldsymbol{e}]$, and $[\boldsymbol{c}]$ are magnetic, magnetoelectric, dielectric, piezomagnetic, piezoelectric, and the elastic constant matrices, respectively. Also, the magnetic and electric fields relating to the magnetic and electric potentials, respectively, are demonstrated with $[\mathcal{H}]$ and $[\mathbf{E}]$. To satisfy Maxwell's equations in the proposed procedure, two assumptions are made: the magnetic field is the negative gradient of $\psi(\mathrm{x}, \mathrm{y}, \mathrm{z}, \mathrm{t})$ and the electric field is the negative gradient of $\Upsilon(\mathrm{x}, \mathrm{y}, \mathrm{z}, \mathrm{t})$. Accordingly, one can write

$$\mathrm{E}_j = -\partial\Upsilon/\partial j, \ \mathcal{H}_j = -\partial\Psi/\partial j, \ \ (j = x, y, z). \tag{8}$$

In view of the boundary conditions at upper and bottom surfaces of each MEE layer, it is possible to combine linear and cosine variations to explicitly describe the electric and magnetic potentials as in [54]

$$\begin{aligned} \Upsilon(x,y,z,t) &= -\cos\left\{\frac{\pi\left[z \pm \left(\frac{h_\mathrm{c}+h_\mathrm{m}}{2}\right)\right]}{h_\mathrm{m}}\right\}\overline{\Upsilon}(x,y,t) + \frac{2\left[z \pm \left(\frac{h_\mathrm{c}+h_\mathrm{m}}{2}\right)\right]\phi_0}{h_\mathrm{m}}, \\ \Psi(x,y,z,t) &= -\cos\left\{\frac{\pi\left[z \pm \left(\frac{h_\mathrm{c}+h_\mathrm{m}}{2}\right)\right]}{h_\mathrm{m}}\right\}\overline{\Psi}(x,y,t) + \frac{2\left[z \pm \left(\frac{h_\mathrm{c}+h_\mathrm{m}}{2}\right)\right]\psi_0}{h_\mathrm{m}}, \end{aligned} \tag{9}$$

where ϕ_0 and ψ_0 denote the determine the initial electric and magnetic potentials on the upper and lower surfaces of each MEE layer, respectively. Furthermore, $\overline{\Psi}$ and $\overline{\Upsilon}$ refer to the two-dimensional magnetic and electric potentials. The vibroacoustic governing equations of motion for double-walled sandwich MEE plate can be obtained using Hamilton's principle as follows

$$\delta\pi = 0, \pi = \int_{t_0}^{t} (\bar{K} - \bar{V} + \bar{W}) dt = 0 \tag{10}$$

where $\bar{V}$, $\bar{W}$ and $\bar{K}$ are the virtual strain energy, the work done by external forces (the work applied by the incidence sound wave and initial electric and magnetic potentials) and kinetic energy, respectively. By taking into account FSDT (Eq. (1)), the kinetic energy for double-walled sandwich MEE plate is expressed as

$$\bar{K} = \sum_{i=1}^{2} \int_{A_i} \left\{ \int_{-h_\mathrm{m}-h_c/2}^{-h_c/2} \rho_\mathrm{m} \left[\left(\dot{U}_i\right)^2 + \left(\dot{V}_i\right)^2 + \left(\dot{W}_i\right)^2 \right] dz + \int_{-h_c/2}^{h_c/2} \rho \left[\left(\dot{U}_i\right)^2 + \left(\dot{V}_i\right)^2 + \left(\dot{W}_i\right)^2 \right] \mathrm{dz} + \int_{-h_c/2}^{h_\mathrm{m}+h_c/2} \rho_\mathrm{m} \left[\left(\dot{U}_i\right)^2 + \left(\dot{V}_i\right)^2 + \left(\dot{W}_i\right)^2 \right] \mathrm{dz} \right\} \mathrm{d}A_i \,, \tag{11}$$

where ρ_m is the mass density of each MEE layer, and A demonstrates the of cross-sectional area. The strain energy double-walled sandwich MEE plate is presented as

$$\begin{aligned} \bar{V} = \sum_{i=1}^{2} \int_{A_i} \Big\{ & \int_{-h_\mathrm{m}-h_c/2}^{-h_c/2} \big(\sigma_{xxi}\varepsilon_{xxi} + \sigma_{yyi}\varepsilon_{yyi} + \tau_{yzi}\gamma_{yzi} + \tau_{xzi}\gamma_{xzi} + \tau_{xyi}\gamma_{xyi} - \\ & D_{xi}\mathrm{E}_{xi} - D_{yi}\mathrm{E}_{yi} - D_{zi}\mathrm{E}_{zi} - B_{xi}\mathcal{H}_{xi} - B_{yi}\mathcal{H}_{yi} - B_{zi}\mathcal{H}_{zi} \big)_\mathrm{m} dz + \int_{-h_c/2}^{h_c/2} \big(\sigma_{xxi}\varepsilon_{xxi} + \\ & \sigma_{yyi}\varepsilon_{yyi} + \tau_{yzi}\gamma_{yzi} + \tau_{xzi}\gamma_{xzi} + \tau_{xyi}\gamma_{xyi} \big) \mathrm{dz} + \int_{-h_c/2}^{h_\mathrm{m}+h_c/2} \big(\sigma_{xxi}\varepsilon_{xxi} + \sigma_{yyi}\varepsilon_{yyi} + \\ & \tau_{yzi}\gamma_{yzi} + \tau_{xzi}\gamma_{xzi} + \tau_{xyi}\gamma_{xyi} - D_{xi}\mathrm{E}_{xi} - D_{yi}\mathrm{E}_{yi} - D_{zi}\mathrm{E}_{zi} - B_{xi}\mathcal{H}_{xi} - B_{yi}\mathcal{H}_{yi} - \\ & B_{zi}\mathcal{H}_{zi} \big)_\mathrm{m} \mathrm{dz} \Big\} \mathrm{d}A_i \,. \end{aligned} \tag{12}$$

The work of nonconservative forces, based on the sound velocity potential, is defined as

$$\begin{aligned} \bar{W} = & \int_{A_1} \left\{ j\omega\rho_0(\Gamma_1 - \Gamma_2) W_{01} + (N_E + N_M) \left[\left(\frac{\partial W_{01}}{\partial x}\right)^2 + \left(\frac{\partial W_{01}}{\partial y}\right)^2 \right] \right\} \mathrm{d}A_1 + \\ & \int_{A_2} \left\{ j\omega\rho_0(\Gamma_2 - \Gamma_3) W_{02} + (N_E + N_M) \left[\left(\frac{\partial W_{02}}{\partial x}\right)^2 + \left(\frac{\partial W_{02}}{\partial y}\right)^2 \right] \right\} \mathrm{d}A_2, \end{aligned} \tag{13}$$

where $N_E = \int_{-h_\mathrm{m}-h_c/2}^{-h_c/2} 2\, e_{31}\, \phi_0/h_\mathrm{m} \mathrm{d}z + \int_{h_c/2}^{h_\mathrm{m}+h_c/2} 2\, e_{31}\, \phi_0/h_\mathrm{m} \mathrm{d}z$ and $N_M = \int_{-h_\mathrm{m}-h_c/2}^{-h_c/2} 2\, f_{31} \psi_0/h_\mathrm{m} \mathrm{d}z + \int_{h_c/2}^{h_\mathrm{m}+h_c/2} 2\, f_{31}\, \psi_0/h_\mathrm{m} \mathrm{d}z$. Also, ω is the angular frequency and ρ_0 expresses air density. Furthermore Γ_1, Γ_2, and Γ_3 express the velocity potentials in the sound incident area, acoustic cavity, and the transmitted acoustic area. The next step is to find the velocity potential. To this aim, the sound waves of any magnitude (positive and negative) are superposed in each zone. The results is written as [55]

$$\begin{aligned} \Gamma_1(x,y,z;t) &= I e^{-j\left(k_{1x}x + k_{1y}y + k_{1z}z - \omega t\right)} + T_1 e^{-j\left(k_{1x}x + k_{1y}y - k_{1z}z - \omega t\right)} \,, \\ \Gamma_2(x,y,z;t) &= T_2 e^{-j\left(k_{2x}x + k_{2y}y + k_{2z}z - \omega t\right)} + T_3 e^{-j\left(k_{2x}x + k_{2y}y - k_{2z}z - \omega t\right)}, \end{aligned} \tag{14}$$

$$\Gamma_3(x,y,z;t) = T_4 e^{-j(k_{3x}x+k_{3y}y+k_{3z}z-\omega t)}$$

in which I refers to the incident sound amplitude and T_1 is the unknown modal coefficient of reflected sound wave in the negative-going incident region. Also T_2 and T_3, respectively, denote the unknown modal coefficients related with positive-going acoustic cavity and negative-going acoustic cavity. Furthermore, the unknown modal coefficient in positive-going transmitted wave is expressed with T_4 and $j = \sqrt{-1}$, and

$$\begin{aligned} &k_{1x} = k_1 \sin\beta_1 \cos\alpha,\ k_{1y} = k_1 \sin\beta_1 \sin\alpha,\ k_{1z} = k_1 \cos\beta_1, \\ &k_{2x} = k_2 \sin\beta_2 \cos\alpha,\ k_{2y} = k_2 \sin\beta_2 \sin\alpha,\ k_{2z} = k_2 \cos\beta_2, \\ &k_{3x} = k_3 \sin\beta_3 \cos\alpha,\ k_{3y} = k_3 \sin\beta_3 \sin\alpha,\ k_{3z} = k_3 \cos\beta_3. \end{aligned} \tag{15}$$

where $k_1 = \frac{\omega}{c_0(1+M\sin\beta_1\cos\alpha)}, k_2 = k_3 = \frac{\omega}{c_0}$ are the air acoustic wavenumbers. Furthermore, c_0 states the air sound velocity and $M = \frac{V}{c_0}$ refers to the Mach number of the external flow. Moreover, in the acoustic cavity and the transmitted fluid region, the directions of sound propagation are as [55]

$$\beta_2 = \arcsin\left(\frac{\sin\beta_1}{1+M\sin\beta_1\cos\alpha}\right),\ \beta_3 = \arcsin\left(\frac{\sin\beta_1}{1+M\sin\beta_1\cos\alpha}\right) \tag{16}$$

Next, substituting Eqs. (11), (12), and (13) into Hamilton's principle (Eq. 10), after performing the required integration by parts in time and space, one ultimately obtains the general vibroacoustic equations of motion for the top and bottom sandwich MEE plates as

$$\begin{aligned} &\delta u_{0i}: \frac{\partial N_{xxi}}{\partial x} + \frac{\partial N_{xyi}}{\partial y} = I_0 \ddot{u}_{0i} + \bar{I}_1 \ddot{\theta}_{xi} - I_3 C_1 \frac{\partial \ddot{W}_{0i}}{\partial x}, \\ &\delta v_{0i}: \frac{\partial N_{xyi}}{\partial x} + \frac{\partial N_{yyi}}{\partial y} = I_0 \ddot{v}_{0i} + \bar{I}_1 \ddot{\theta}_{yi} - I_3 C_1 \frac{\partial \ddot{W}_{0i}}{\partial y}, \\ &\delta W_{0i}: \frac{\partial Q_{xzi}}{\partial x} + \frac{\partial Q_{yzi}}{\partial y} - 3C_1\left(\frac{\partial R_{xzi}}{\partial x} + \frac{\partial R_{yzi}}{\partial y}\right) + C_1\left(\frac{\partial^2 P_{xxi}}{\partial x^2} + 2\frac{\partial^2 P_{xyi}}{\partial x \partial y} + \frac{\partial^2 P_{yyi}}{\partial y^2}\right) = q_i + \\ &I_0 \ddot{W}_{0i} + I_3 C_1\left(\frac{\partial \ddot{u}_{0i}}{\partial x} + \frac{\partial \ddot{v}_{0i}}{\partial y}\right) - I_6 C_1^2\left(\frac{\partial^2 \ddot{W}_{0i}}{\partial x^2} + \frac{\partial^2 \ddot{W}_{0i}}{\partial y^2}\right) + \bar{I}_4 C_1\left(\frac{\partial \ddot{\theta}_{xi}}{\partial x} + \frac{\partial \ddot{\theta}_{yi}}{\partial y}\right) - (N_E + \\ &N_M)\left(\frac{\partial^2 W_{0i}}{\partial x^2} + \frac{\partial^2 W_{0i}}{\partial y^2}\right), \\ &\delta \theta_{xi}: \frac{\partial M_{xxi}}{\partial x} + \frac{\partial M_{xyi}}{\partial y} - C_1\left(\frac{\partial P_{xxi}}{\partial x} + \frac{\partial P_{xyi}}{\partial y}\right) - Q_{xzi} + 3C_1 R_{xzi} = \bar{I}_1 \ddot{u}_{0i} + \bar{I}_2 \ddot{\theta}_{xi} - \\ &C_1 \bar{I}_4 \frac{\partial \ddot{W}_{0i}}{\partial x}, \end{aligned} \tag{17}$$

$$\delta\theta_{yi}: \frac{\partial M_{yyi}}{\partial y} + \frac{\partial M_{xyi}}{\partial x} - C_1\left(\frac{\partial P_{yyi}}{\partial y} + \frac{\partial P_{xyi}}{\partial x}\right) - Q_{yzi} + 3C_1R_{yzi} = \bar{I}_1\ddot{v}_{0i} + \bar{I}_2\ddot{\theta}_{yi} - C_1\bar{I}_4\frac{\partial \ddot{W}_{0i}}{\partial y},$$

$$\delta\bar{\Upsilon}_i: \int_{-h_m-h_c/2}^{-h_c/2}\left(\frac{\partial D_{xi}}{\partial x}\cos\left\{\frac{\pi\left[z+\left(\frac{h_c+h_m}{2}\right)\right]}{h_m}\right\} + \frac{\partial D_{yi}}{\partial y}\cos\left\{\frac{\pi\left[z+\left(\frac{h_c+h_m}{2}\right)\right]}{h_m}\right\} + \frac{\pi}{h_m}D_{zi}\sin\left\{\frac{\pi\left[z+\left(\frac{h_c+h_m}{2}\right)\right]}{h_m}\right\}\right)dz + \int_{h_c/2}^{h_m+h_c/2}\left(\frac{\partial D_{xi}}{\partial x}\cos\left\{\frac{\pi\left[z-\left(\frac{h_c+h_m}{2}\right)\right]}{h_m}\right\} + \frac{\partial D_{yi}}{\partial y}\cos\left\{\frac{\pi\left[z-\left(\frac{h_c+h_m}{2}\right)\right]}{h_m}\right\} + \frac{\pi}{h_m}D_{zi}\sin\left\{\frac{\pi\left[z-\left(\frac{h_c+h_m}{2}\right)\right]}{h_m}\right\}\right) = 0,$$

$$\delta\bar{\Psi}_i: \int_{-h_m-h_c/2}^{-h_c/2}\left(\frac{\partial B_{xi}}{\partial x}\cos\left\{\frac{\pi\left[z+\left(\frac{h_c+h_m}{2}\right)\right]}{h_m}\right\} + \frac{\partial B_{yi}}{\partial y}\cos\left\{\frac{\pi\left[z+\left(\frac{h_c+h_m}{2}\right)\right]}{h_m}\right\} + \frac{\pi}{h_m}B_{zi}\sin\left\{\frac{\pi\left[z+\left(\frac{h_c+h_m}{2}\right)\right]}{h_m}\right\}\right)dz + \int_{h_c/2}^{h_m+h_c/2}\left(\frac{\partial B_{xi}}{\partial x}\cos\left\{\frac{\pi\left[z-\left(\frac{h_c+h_m}{2}\right)\right]}{h_m}\right\} + \frac{\partial B_{yi}}{\partial y}\cos\left\{\frac{\pi\left[z-\left(\frac{h_c+h_m}{2}\right)\right]}{h_m}\right\} + \frac{\pi}{h_m}B_{zi}\sin\left\{\frac{\pi\left[z-\left(\frac{h_c+h_m}{2}\right)\right]}{h_m}\right\}\right) = 0,$$

where $i = 1,2$ and $q_1 = j\omega\rho_0(\Gamma_1 - \Gamma_2)$, $q_2 = j\omega\rho_0(\Gamma_2 - \Gamma_3)$. Furthermore, the resultant momentum $N_{xx}, N_{xy}, N_{yy}, M_{xx}, M_{xy}, M_{yy}, Q_{xz}, Q_{yz}$ and mass inertia terms $I_0, I_1, I_2, I_3, I_4, I_6$ are written as

$$\{N_{xxi}, N_{yyi}, N_{xyi}\} = \int_{-h_m-h_c/2}^{-h_c/2}\{\sigma_{xxi}, \sigma_{yyi}, \tau_{xyi}\}_m dz + \int_{-h_c/2}^{h_c/2}\{\sigma_{xxi}, \sigma_{yyi}, \tau_{xyi}\}_{PFGM} dz + \int_{h_c/2}^{h_c/2+h_m}\{\sigma_{xxi}, \sigma_{yyi}, \tau_{xyi}\}_m dz,$$

$$\{M_{xxi}, M_{yyi}, M_{xyi}\} = \int_{-h_m-h_c/2}^{-h_c/2}\{\sigma_{xxi}, \sigma_{yyi}, \tau_{xyi}\}_m z dz + \int_{-h_c/2}^{h_c/2}\{\sigma_{xxi}, \sigma_{yyi}, \tau_{xyi}\}_{PFGM} z dz + \int_{h_c/2}^{h_c/2+h_m}\{\sigma_{xxi}, \sigma_{yyi}, \tau_{xyi}\}_m z dz, \quad (18)$$

$$\{P_{xxi}, P_{yyi}, P_{xyi}\} = \int_{-h_m-h_c/2}^{-h_c/2}\{\sigma_{xxi}, \sigma_{yyi}, \tau_{xyi}\}_m z^3 dz + \int_{-h_c/2}^{h_c/2}\{\sigma_{xxi}, \sigma_{yyi}, \tau_{xyi}\}_{PFGM} z^3 dz + \int_{h_c/2}^{h_c/2+h_m}\{\sigma_{xxi}, \sigma_{yyi}, \tau_{xyi}\}_m z^3 dz,$$

$$\{Q_{xzi}, Q_{yzi}\} = \left[\int_{-h_m-h_c/2}^{-h_c/2}\{\tau_{xzi}, \tau_{yzi}\}_m dz + \int_{-h_c/2}^{h_c/2}\{\tau_{xzi}, \tau_{yzi}\}_{PFGM} dz + \int_{h_c/2}^{h_c/2+h_m}\{\tau_{xzi}, \tau_{yzi}\}_m dz\right],$$

$$\{R_{xzi}, R_{yzi}\} = \left[\int_{-h_m-h_c/2}^{-h_c/2}\{\tau_{xzi}, \tau_{yzi}\}_m z^2 dz + \int_{-h_c/2}^{h_c/2}\{\tau_{xzi}, \tau_{yzi}\}_{PFGM} z^2 dz + \int_{h_c/2}^{h_c/2+h_m}\{\tau_{xzi}, \tau_{yzi}\}_m z^2 dz\right]$$

$$\{I_0, I_1, I_2, I_3, I_4, I_6\} = \int_{-h_m-h_c/2}^{-h_c/2}\rho_m\{1, z, z^2, z^3, z^4, z^6\}dz + \int_{-h_c/2}^{h_c/2}\rho(z)\{1, z, z^2, z^3, z^4, z^6\}_{PFGM}dz + \int_{h_c/2}^{h_c/2+h_m}\rho_m\{1, z, z^2, z^3, z^4, z^6\}dz,$$

$$\bar{I}_1 = I_1 - I_3C_1,\ \bar{I}_2 = I_2 - 2C_1I_4 + C_1^2I_6,\ \bar{I}_4 = I_4 - C_1I_6.$$

where $i = 1,2$. Finally, substituting Eq. (18) (with respect to Eqs. (3) and (4)) into Eq. (17), the equilibrium equation in terms of displacement is derived and detailed in Appendix A.

To analytically solving the governing equation of motion (A1-A7), the boundary conditions of all four edges of each sandwich MEE plate are supposed to be simply supported. Therefore, the displacement and moment conditions are presented as

$$\begin{aligned}
&u_{0i}(x,0,t) = u_{0i}(x,b,t) = v_{0i}(0,y,t) = v_{0i}(a,y,t) = 0,\\
&W_{0i}(x,0,t) = W_{0i}(x,b,t) = W_{0i}(0,y,t) = W_{0i}(a,y,t) = 0,\\
&\theta_{xi}(x,0,t) = \theta_{xi}(x,b,t) = \theta_{yi}(0,y,t) = \theta_{yi}(a,y,t) = 0,\\
&\overline{\Upsilon}_i(x,0,\tau) = \overline{\Upsilon}_i(x,b,t) = \overline{\Psi}_i(0,y,t) = \overline{\Psi}_i(a,y,t) = 0,\\
&\overline{\Upsilon}_i(0,y,\tau) = \overline{\Upsilon}_i(a,y,t) = \overline{\Psi}_i(x,0,t) = \overline{\Psi}_i(x,b,t) = 0,\\
&M_{xxi}(0,y,t) = M_{xxi}(a,y,t) = M_{yyi}(x,0,t) = M_{yyi}(x,b,t) = 0,\\
&P_{xxi}(0,y,t) = P_{xxi}(a,y,t) = P_{yyi}(x,0,t) = P_{yyi}(x,b,t) = 0,
\end{aligned} \tag{19}$$

where $i = 1,2$. To satisfy simply supported boundary condition, based on Navier-solution approach, the following deflection components for each sandwich MEE plate are defined

$$\begin{aligned}
&\{u_{0i}, \theta_{xi}\} = \sum_{m=1}^{\infty}\sum_{n=1}^{\infty}\cos(m\pi x/a)\sin(n\pi y/b)\{\tilde{u}_i, \tilde{\theta}_{xi}\}e^{j\omega t},\\
&\{v_{0i}, \theta_{yi}\} = \sum_{m=1}^{\infty}\sum_{n=1}^{\infty}\sin(m\pi x/a)\cos(n\pi y/b)\{\tilde{v}_i, \tilde{\theta}_{yi}\}e^{j\omega t},\\
&\{W_{0i}, \overline{\Upsilon}_i, \overline{\Psi}_i\} = \sum_{m=1}^{\infty}\sum_{n=1}^{\infty}\sin(m\pi x/a)\sin(n\pi y/b)\{\widetilde{w}_i, \widetilde{\Upsilon}_i, \widetilde{\Psi}_i\}e^{j\omega t},
\end{aligned} \tag{20}$$

where $i = 1,2$ and m and n are, respectively, the half wave numbers along x and y directions. Furthermore, $\tilde{u}_i, \tilde{\theta}_{xi}, \tilde{v}_i, \tilde{\theta}_{yi}, \widetilde{w}_i, \widetilde{\Upsilon}_i, \widetilde{\Psi}_i$ signify the unknown modal coefficients related to the upper and bottom sandwich MEE plates, respectively.

2.2. *Acoustic model*

One can define the velocity potential at this stage for the three acoustic zones (Γ_1: incident zone, Γ_2: enclosure, and Γ_3: transmission zone) using the transverse modal function $A_{mn} = \sin(m\pi x/a)\sin(n\pi y/b)$ with respect to Eq. (14) for the sandwich panel according to [55]

$$\Gamma_1(x,y,z;t) = \sum_{m=1}^{\infty}\sum_{n=1}^{\infty} I_{mn}A_{mn}(x,y)e^{-j(k_{1z}z-\omega t)} + \sum_{m=1}^{\infty}\sum_{n=1}^{\infty} T_1 A_{mn}(x,y)e^{-j(-k_{1z}z-\omega t)}, \tag{21}$$

$$\Gamma_1(x,y,z;t) = \sum_{m=1}^{\infty}\sum_{n=1}^{\infty} T_2 A_{mn}(x,y)e^{-j(k_{2z}z-\omega t)} + \sum_{m=1}^{\infty}\sum_{n=1}^{\infty} T_3 A_{mn}(x,y)e^{-j(-k_{2z}z-\omega t)},$$

$$\Gamma_1(x,y,z;t) = \sum_{m=1}^{\infty}\sum_{n=1}^{\infty} T_4 A_{mn}(x,y)e^{-j(k_{3z}z-\omega t)}$$

To describe the modal amplitude of the plate corresponding to impingent wave, one should exploit the ordinary orthogonality equations of modal functions. The details of this procedure are expressed as $I_{mn} = 4(I_0/ab)\int_0^a\int_0^b e^{-j(k_{1x}x+k_{1y}y)}\sin(m\pi x/a)\sin(n\pi y/b)\mathrm{d}y\mathrm{d}x$, which I_0 denotes the amplitude of incident wave.

To determine the coefficients (T_1, T_2, T_3, T_4), it is imperative to concurrently satisfy the continuity conditions for the normal velocity components at the boundary of fluid and structure for the top and bottom surfaces of each sandwich MEE plate as

$$\rho_0 j\omega \frac{\partial\Gamma_1}{\partial z}\bigg|_{z=L+2h_\mathrm{m}+h_\mathrm{c}} = \rho_0\left(\frac{\partial}{\partial t}+V\frac{\partial}{\partial x}\right)^2 W_{01}, \quad \rho_0 j\omega \frac{\partial\Gamma_2}{\partial z}\bigg|_{z=L} = \rho_0\frac{\partial^2 W_{01}}{\partial t^2}, \tag{22}$$

$$\rho_0 j\omega \frac{\partial\Gamma_2}{\partial z}\bigg|_{z=0} = \rho_0\frac{\partial^2 W_{02}}{\partial t^2}, \quad \rho_0 j\omega \frac{\partial\Gamma_3}{\partial z}\bigg|_{z=-(2h_\mathrm{m}+h_\mathrm{c})} = \rho_0\frac{\partial^2 W_{02}}{\partial t^2}.$$

Substituting equations (20) and (21) in equation (22) yields the next important equations:

$$T_1 = I_{mn}e^{-2jk_{1z}(L+2h_\mathrm{m}+h_\mathrm{c})} - (\omega - Vk_{1x})^2\frac{\tilde{w}_1 e^{-jk_{1z}(L+2h_\mathrm{m}+h_\mathrm{c})}}{k_{1x}k_{1z}}, T_2 = \omega\frac{(\tilde{w}_1-\tilde{w}_2 e^{jk_{2z}L})}{k_{2z}(e^{-jk_{2z}L}-e^{jk_{2z}L})}, \; T_3 = \omega\frac{(\tilde{w}_1-\tilde{w}_2 e^{-jk_{2z}L})}{k_{2z}(e^{-jk_{2z}L}-e^{jk_{2z}L})}, \; T_4 = \omega\frac{\tilde{w}_2 e^{-jk_{3z}(2h_\mathrm{m}+h_\mathrm{c})}}{k_{3z}}. \tag{23}$$

To derive the matrix format of the equilibrium equations, one should implement Eqs. (20)–(21) in the developed governing relations described in (A1-A7). The results are presented here as in

$$
\begin{bmatrix}
\mathcal{L}_{1,1} & \mathcal{L}_{1,2} & \mathcal{L}_{1,3} & \mathcal{L}_{1,4} & \mathcal{L}_{1,5} & \mathcal{L}_{1,6} & \mathcal{L}_{1,7} & 0 & 0 & 0 & 0 & 0 & 0 & 0 \\
\mathcal{L}_{2,1} & \mathcal{L}_{2,2} & \mathcal{L}_{2,3} & \mathcal{L}_{2,4} & \mathcal{L}_{2,5} & \mathcal{L}_{2,6} & \mathcal{L}_{2,7} & 0 & 0 & 0 & 0 & 0 & 0 & 0 \\
\mathcal{L}_{3,1} & \mathcal{L}_{3,2} & \mathcal{L}_{3,3} & \mathcal{L}_{3,4} & \mathcal{L}_{3,5} & \mathcal{L}_{3,6} & \mathcal{L}_{3,7} & 0 & 0 & \mathcal{L}_{3,10} & 0 & 0 & 0 & 0 \\
\mathcal{L}_{4,1} & \mathcal{L}_{4,2} & \mathcal{L}_{4,3} & \mathcal{L}_{4,4} & \mathcal{L}_{4,5} & \mathcal{L}_{4,6} & \mathcal{L}_{4,7} & 0 & 0 & 0 & 0 & 0 & 0 & 0 \\
\mathcal{L}_{5,1} & \mathcal{L}_{5,2} & \mathcal{L}_{5,3} & \mathcal{L}_{5,4} & \mathcal{L}_{5,5} & \mathcal{L}_{5,6} & \mathcal{L}_{5,7} & 0 & 0 & 0 & 0 & 0 & 0 & 0 \\
\mathcal{L}_{6,1} & \mathcal{L}_{6,2} & \mathcal{L}_{6,3} & \mathcal{L}_{6,4} & \mathcal{L}_{6,5} & \mathcal{L}_{6,6} & \mathcal{L}_{6,7} & 0 & 0 & 0 & 0 & 0 & 0 & 0 \\
\mathcal{L}_{7,1} & \mathcal{L}_{7,2} & \mathcal{L}_{7,3} & \mathcal{L}_{7,4} & \mathcal{L}_{7,5} & \mathcal{L}_{7,6} & \mathcal{L}_{7,7} & 0 & 0 & 0 & 0 & 0 & 0 & 0 \\
0 & 0 & 0 & 0 & 0 & 0 & 0 & \mathcal{L}_{8,8} & \mathcal{L}_{8,9} & \mathcal{L}_{8,10} & \mathcal{L}_{8,11} & \mathcal{L}_{8,12} & \mathcal{L}_{8,13} & \mathcal{L}_{8,14} \\
0 & 0 & 0 & 0 & 0 & 0 & 0 & \mathcal{L}_{9,8} & \mathcal{L}_{9,9} & \mathcal{L}_{9,10} & \mathcal{L}_{9,11} & \mathcal{L}_{9,12} & \mathcal{L}_{9,13} & \mathcal{L}_{9,14} \\
0 & 0 & \mathcal{L}_{10,3} & 0 & 0 & 0 & 0 & \mathcal{L}_{10,8} & \mathcal{L}_{10,9} & \mathcal{L}_{10,10} & \mathcal{L}_{10,11} & \mathcal{L}_{10,12} & \mathcal{L}_{10,13} & \mathcal{L}_{10,14} \\
0 & 0 & 0 & 0 & 0 & 0 & 0 & \mathcal{L}_{11,8} & \mathcal{L}_{11,9} & \mathcal{L}_{11,10} & \mathcal{L}_{11,11} & \mathcal{L}_{11,12} & \mathcal{L}_{11,13} & \mathcal{L}_{11,14} \\
0 & 0 & 0 & 0 & 0 & 0 & 0 & \mathcal{L}_{12,8} & \mathcal{L}_{12,9} & \mathcal{L}_{12,10} & \mathcal{L}_{12,11} & \mathcal{L}_{12,12} & \mathcal{L}_{12,13} & \mathcal{L}_{12,14} \\
0 & 0 & 0 & 0 & 0 & 0 & 0 & \mathcal{L}_{13,8} & \mathcal{L}_{13,9} & \mathcal{L}_{13,10} & \mathcal{L}_{13,11} & \mathcal{L}_{13,12} & \mathcal{L}_{13,13} & \mathcal{L}_{13,14} \\
0 & 0 & 0 & 0 & 0 & 0 & 0 & \mathcal{L}_{14,8} & \mathcal{L}_{14,9} & \mathcal{L}_{14,10} & \mathcal{L}_{14,11} & \mathcal{L}_{14,12} & \mathcal{L}_{14,13} & \mathcal{L}_{14,14}
\end{bmatrix}
\begin{bmatrix}
\tilde{u}_1 \\ \tilde{v}_1 \\ \tilde{w}_1 \\ \tilde{\theta}_{x1} \\ \tilde{\theta}_{y1} \\ \tilde{\Upsilon}_1 \\ \tilde{\Psi}_1 \\ \tilde{u}_2 \\ \tilde{v}_2 \\ \tilde{w}_2 \\ \tilde{\theta}_{x2} \\ \tilde{\theta}_{y2} \\ \tilde{\Upsilon}_2 \\ \tilde{\Psi}_2
\end{bmatrix}
=
\begin{bmatrix}
0 \\ 0 \\ F \\ 0 \\ 0 \\ 0 \\ 0 \\ 0 \\ 0 \\ 0 \\ 0 \\ 0 \\ 0 \\ 0
\end{bmatrix}
\tag{24}
$$

where $\mathcal{L}_{i,j}$ and F are expressed in Appendix B.

2.3. STL formulation

Inversing the power transmission coefficient, actually yields a highly-used quantity known as sound transmission loss or STL usually described in dB. Regarding the double-panel domain, one can obtain [46]

$$
STL = 10log_{10}\left(\frac{\sum_{m=1}^{\infty}\sum_{n=1}^{\infty}|I_{mn}+T_1|^2}{\sum_{m=1}^{\infty}\sum_{n=1}^{\infty}|T_4|^2}\right), \tag{25}
$$

3. Numeric investigation

The numerical findings are provided here. Before presenting them, however, it is best to compare sample results to the available data in certain studies. However, Table 1 lists different parameters employed hereafter (not including the verification part).

3.1. Convergence checking

As delineated earlier, owing to the use of double Fourier series as the employed solution approach, one needs to select an adequate number of modes for the series to attain an accurate answer. To guarantee such a condition, a trial-and-error scheme is implemented. For this purpose, the values of *m* and *n* are augmented and the stability in the estimated STL is examined. For a normal impingent sound wave, and type C of the porosity configurations, and different frequencies, Fig. 2 demonstrates the convergence of obtained STL in the double-walled sandwich MEE square plate when $a = b = 0.8\text{m}, L = 3\text{cm}, h_{\text{m}} = 0.5\text{mm}, h_{\text{c}} = 1\text{mm}, \beta_1 = 30^{\circ}, \phi_0 = 0, \psi_0 = 0, e_0 = 0.1, M = 0, p = 1$. As evident in the figure, 1600 terms ($m = 40$ and $n = 40$) appear to secure the convergence of results.

3.2. Verification study

A series of comparisons are made here to show whether the developed procedure is accurate enough.

As a first verification study, by disregarding the properties of PFGM core in their respective systems, the first nondimensional natural frequency ($\widetilde{\omega}_{11} = \omega_{11} a^2 \sqrt{\rho_{\mathrm{m}}/c_{11}}$) of a rectangular MEE plate for different aspect ratios are obtained in Table 2, which are then compared and validated against the results reported in Refs. [56,57].

In another comparison investigation, by neglecting MEE layers, sound wave, porosity, the variation of the first three dimensionless natural frequencies of the FGM plate ($a\ /\ b = 1, a = 10h$) are calculated based on the present model and then compared with the results of Ref. [58] as presented in Table 3. The comparison made in this table indicates that the current results are in good agreement with analytical predictions of Ref. [58].

Finally, by eliminating MEE layers, for the normal incident sound ($\beta_1 = 0^{\circ}$), the STL through double-walled elastic square plate is obtained by the presented formulation and is compared with those predicted based CPT by Ref. [59] in Fig. 3 when $E = 70GPa$, $\rho = 2700\mathrm{Kg/m^3}$, $\vartheta = 0.3, a = b = 0.3\mathrm{m}, L = 80\mathrm{mm}, h_{\mathrm{c}} = 1\mathrm{mm}$. It is observed that an acceptable agreement exists between the results.

3.3.Main results

The proper understanding of the impacts of effective parameters on the STL in the double-walled sandwich MEE-PFGM plate is realized here using a series of numerical studies. The considered quantities include plate and cavity dimensions, initial magnetic and electric potentials, elevation angle.

Fig. 4. depicts the STL curves against the frequency interval through single/double-walled sandwich MEE-PFGM plate of finite/infinite extent for when $a = b = 0.8\mathrm{m}, L = 3\mathrm{cm}, h_{\mathrm{m}} = 0.5\mathrm{mm}, h_{\mathrm{c}} = 1\mathrm{mm}, \beta_1 = 30^{\circ}, \phi_0 = 0, \psi_0 = 0, e_0 = 0.1, M = 0, p = 1$. It should be noted that the "mass-air-mass" resonance dip ($\mathrm{f_m}$) in Fig. 4 is marked which is a unique phenomenon owned by the double-panel system and can be approximately predicted by the formula [53]

$$\mathrm{f_m} = (1/2\pi cos\beta_2)\{(\rho_0\, {c_0}^2\, [(I_0\,)_{plate1} + (I_0)_{plae2}])/L[(I_0)_{plate1} \times (I_0\,)_{plate2}\,]\}^{1/2}. \quad (26)$$

One should note that the condition for mass-air-mass resonance is the resonance of two MEE-PFGM panels over the stiffness of the splitting layer of air, resulting in a frequency interval of unsatisfactory STL. Furthermore, at higher frequencies, the resonance dips indicated with $\mathrm{f_s}$ are the related to the standing-wave resonance phenomenon (i.e. $\mathrm{f_s} = \frac{ic_0}{2Lsin\,\beta_2}$) that happen when "the distance difference between the routes that the two intervening waves pass through is the multiple of the half wavelength of the incidence sound wave" [45]. It can be observed that the number of

resonances of the finite double plate partitions surpasses that of the finite single plate. This is attributed to the effects of acoustic cavity between the two plates. In addition, the dips prior to "mass-air-mass" resonance represent the system natural frequencies which are the same for double and single panels irrespective of the acoustic cavity. It is also of central importance that greater plate dimensions result in smoother STL response such that the number of dips/peaks reaches a minimum. Also, Regarding the STL-frequency plot of the double plate with infinite dimensions, an upper bound for the partitions of finite size is dictated after the "mass-air-mass" resonance dip, as the panel mode-dominated STL disappears for this special case. Nonetheless, for frequencies smaller than the "mass-air-mass" resonance dip, the noise-cancellation efficiency of the structure with infinite dimensions is not up to par compared to the finite system. This is a direct result of boundary constraints.

Fig. 5 indicates the variations of the STL across the sandwich double MEE-PFGM plate versus different values of the material gradient index for type C of the porosity configurations when $a = b = 0.8\text{m}, L = 3\text{cm}, h_\text{m} = 0.5\text{mm}, h_\text{c} = 1\text{mm}, \beta_1 = 30^\circ, \phi_0 = 0, \psi_0 = 0, e_0 = 0.1, M = 0$. As a result, the change from ceramic to metallic state, which indicates a growth in FGM index and a decrease in stiffness, reduces the dimensionless natural frequency. Furthermore, before the "mass-air-mass" resonance dip, an increase in the material gradient index improves the STL performance. Moreover, by increasing the material gradient index, the location of the "mass-air-mass" resonance dip shifts downward which is linked to the increased equivalent mass density (see equation (26)).

Figure 6a and b describes the effects of different porosity coefficients for all types of porosity distribution on the variation of STL through double-walled sandwich MEE-PFGM plate when $a = b = 0.8\text{m}, L = 3\text{cm}, h_\text{m} = 0.5\text{mm}, h_\text{c} = 1\text{mm}, \beta_1 = 30^\circ, \phi_0 = 0, \psi_0 = 0, M = 0, p = 1$. However, it can be observed that with increasing porosity coefficient, STL curves of the system decreases in all cases of porosity distributions. This behavior is attributed to the reduction in structural stiffness of the system with increasing porosity. However, it seems that different porosity configurations have a little effect on the changes of the STL.

The influence of the external flow Mach number on the STL through the sandwich double MEE-PFGM plate for type C of the porosity configurations is displayed in Fig. 7 when $a = b = 0.8\text{m}, L = 3\text{cm}, h_\text{m} = 0.5\text{mm}, h_\text{c} = 1\text{mm}, \beta_1 = 30^\circ, \phi_0 = 0, \psi_0 = 0, e_0 = 0.1$. It can be observed that by increasing the external flow Mach number, the STL value significantly improves in the resonances. This behavior is due to this fact that a convective fluid loading is exerted on the structure because of the presence of external mean flow, which decreases the sound energy transmitted through the panel system and increases the sound energy reflected.

Fig. 8 displays the effects of the external electric potential on the changes of STL across double-walled sandwich MEE-PFGM plate for type C of the porosity configurations when $a = b = 0.8\text{m}, L = 3\text{cm}, h_\text{m} = 0.5\text{mm}, h_\text{c} = 1\text{mm}, \beta_1 = 30^\circ, \psi_0 = 0, e_0 = 0.1, M = 0$. Notably, soundproofing efficiency can be enhanced by increasing the external voltage. This is particularly

true for low-frequency intervals of "mass-air-mass" resonance. Furthermore, as can be expected the, the location of "mass-air-mass" resonance is independent of applied electric potential.

In order to study the effect of external magnetic potential on the STL curves of double-walled sandwich MEE-PFGM plate, Fig. 9 is presented for type C of the porosity configurations when $a = b = 0.8\text{m}, L = 3\text{cm}, h_\text{m} = 0.5\text{mm}, h_\text{c} = 1\text{mm}, \beta_1 = 30^\circ, \phi_0 = 0, M = 0, e_0 = 0.1$. As can be seen, the values of ST can be enhanced by increasing the external magnetic potential specially before "mass-air-mass" resonance dip. This is particularly true for low-frequency intervals of "mass-air-mass" resonance. Furthermore, as can be expected the, the location of "mass-air-mass" resonance is independent of initial magnetic potential. A careful examination of this figure reveals that the effect of external magnetic potential on the improvement of STL is more significant than that of electric voltage.

Depicted in Fig. 10 is the influence of air cavity depth on the STL curves of double-walled sandwich MEE-PFGM plate for type C of the porosity configurations when $a = b = 0.8\text{m}, L = 3\text{cm}, h_\text{m} = 0.5\text{mm}, h_\text{c} = 1\text{mm}, \beta_1 = 30^\circ, \psi_0 = 0, \phi_0 = 0, M = 0, e_0 = 0.1$. As previously expressed, the acoustic cavity has no effect on the resonances of double plate in the frequency region prior to "mass-air-mass" resonance. Adding to the depth of air cavity significantly alters the behavior of STL with respect to frequency. For those frequencies greater than the "mass-air-mass" resonance, one observes that greater depths are accompanied with higher STLs. The "mass-air-mass" resonance dips tend to move downwards as the air cavity deepens. This behavior is explained by the smaller equivalent stiffness associated with cavities.

Fig. 11 indicates the variations of STL double-walled sandwich MEE-PFGM plate for different values of elevation angle and type C of the porosity configurations when $a = b = 0.8\text{m}, L = 3\text{cm}, h_\text{m} = 0.5\text{mm}, h_\text{c} = 1\text{mm}, \psi_0 = 0, \phi_0 = 0, M = 0, e_0 = 0.1$. The direct relationship between the elevation angle and the "mass-air-mass" resonance is also observed here. Reduced values of the elevation angle of impingent sound waves arguably improve the noise-cancellation of the studied system for all frequencies. Also noteworthy is that a large elevation angle for an incoming sound wave leads to its easier transmission through the double-walled sandwich plate. In addition, since the plate mode is shown to be independent of impingent elevation angle, dips prior to the "mass-air-mass" resonance remains constant with respect to elevation angle.

Fig. 12 exhibits the effects of sandwich MEE-PFGM plate thickness on STL curves for type C of the porosity configurations when $a = b = 0.8\text{m}, L = 3\text{cm}, \beta_1 = 30^\circ, \psi_0 = 0, \phi_0 = 0, M = 0, e_0 = 0.1$. Clearly, the noise-cancellation behavior of the plate is highly affected by the ratio of sandwich plate thickness. As expected from the mass law, the STL improves from both the increased thickness of single panel and the coupling impacts of air cavity, with the latter playing a more prominent role. Furthermore, the declining move of "mass-air-mass" resonance with growing thickness originates from the higher plate surface density.

4. Conclusions

The Third-order shear deformation theory and three cases of uneven porosity distribution pattern are applied to study the sound transmission loss through the air-filled double-walled sandwich magneto-electro-elastic plate with porous functionally graded material core layer subjected to the initial external electric and magnetic potentials, and external mean airflow. The material characteristics of PFGM core layer change slowly through the thickness via power-law scheme. The coupled vibroacoustic governing equations are obtained using Hamilton's principle in conjunction with the normal fluid/structure velocity components. The effects of different significant parameters on the sound transmission loss of the structure over certain frequency intervals, particularly the important region of "mass-air-mass" resonance, are investigated. Some of the most important results of this study are listed in the following.

- The values of ST can be enhanced by increasing the external electric and magnetic potentials specially before "mass-air-mass" resonance dip.
- By increasing the external flow Mach number, the STL value significantly improves in the resonances.
- With increasing porosity coefficient, STL values of the system decreases in all cases of porosity distributions.
- Before the "mass-air-mass" resonance dip, an increase in the material gradient index improves the STL performance
- STL improves from both the increased thickness of single panel and the coupling impacts of air cavity, with the latter playing a more prominent role.
- The "mass-air-mass" resonance dips tend to move downwards as the air cavity deepens. This behavior is explained by the smaller equivalent stiffness associated with cavities.

Table caption

Table 1. Material properties of the MEE-PFGM plate and acoustic medium.

Table 2. Comparison of dimensionless natural frequency of a MEE plate.

Table 3. Comparison of dimensionless natural frequency of a FGM plate.

.

Figure Caption

Fig. 1. The schematic of double-walled MEE-PFGM plate under incidence wave and external mean airflow.

Fig. 2. Mode convergence diagram for double-walled MEE-PFGM plate.

Fig. 3. Comparison study of STL curves for double-walled elastic plate.

Fig. 4. The variations of STL through single/double-walled MEE-PFGM plate versus plate dimensions.

Fig. 5. Effect of the material gradient index on the STL through double-walled MEE-PFGM plate.

Fig. 6. The STL of double-walled MEE-PFGM plate (a): against the porosity distribution models; (b) against the porosity coefficient.

Fig. 7. The effect of the external flow Mach number on the STL of double-walled MEE-PFGM plate.

Fig. 8. The effect of the external electric potential on the changes of STL through double-walled MEE-PFGM plate.

Fig. 9. The effect of the external magnetic potential on the changes of STL through double-walled MEE-PFGM plate.

Fig. 10. The effect of the air cavity depth on STL curves of double-walled MEE-PFGM plate.

Fig. 11. The effect of elevation angle on STL curves of double-walled MEE-PFGM plate.

Fig. 12. The effect of sandwich MEE-PFGM plate thickness on the variations of STL.

Acknowledgements

This study was supported by Thammasat Postdoctoral Fellowship, Thammasat University Research Division, Thammasat University. Also, this Research was supported by Thammasat University Research Unit in Structural and Foundation Engineering, Thammasat University.

Funding: This research received no external funding.

Data Availability

The datasets generated during the current study are available from the below listed authors on reasonable request:

Peyman Roodgar Saffari: *rpeyman@engr.tu.ac.th*

Nima Refahati: refahati@damavandiau.ac.ir

Pouyan Roodgar Saffari: *poyan.safari31@gmail.com*

References

[1] D. Chen, S. Kitipornchai, J. Yang, Dynamic response and energy absorption of functionally graded porous structures, Mater. Des. 140 (2018) 473–487.

[2] J. Zhou, A. Bhaskar, X. Zhang, The effect of external mean flow on sound transmission through double-walled cylindrical shells lined with poroelastic material, J. Sound Vib. 333 (2014) 1972–1990. https://doi.org/10.1016/J.JSV.2013.11.038.

[3] D. Chen, J. Yang, S. Kitipornchai, Free and forced vibrations of shear deformable functionally graded porous beams, Int. J. Mech. Sci. 108 (2016) 14–22.

[4] Y.Q. Wang, J.W. Zu, Porosity-dependent nonlinear forced vibration analysis of functionally graded piezoelectric smart material plates, Smart Mater. Struct. 26 (2017) 105014.

[5] F. Ebrahimi, D. Hashemabadi, M. Habibi, H. Safarpour, Thermal buckling and forced vibration characteristics of a porous GNP reinforced nanocomposite cylindrical shell, Microsyst. Technol. 26 (2020) 461–473.

[6] G. Pourmoosavi, S.A.M. Ghasemi, B.F. Azar, S. Talatahari, Shear design curves of unstiffened plate girder web panels at high temperatures, J. Constr. Steel Res. 164 (2020) 105808.

[7] G.H. Pourmoosavi, S.A.M. Ghasemi, B.F. Azar, S. Talatahari, Numerical investigation on ultimate shear strength of long steel plate girder web panels at high temperatures, J. Build. Eng. 29 (2020) 101070.

[8] Y.H. Song, E.K. Ji, B.W. Jeong, M.K. Jung, E.Y. Kim, D.H. Yoon, High power laser-driven ceramic phosphor plate for outstanding efficient white light conversion in application of automotive lighting, Sci. Rep. 6 (2016) 1–7.

[9] L. Yang, Y. Guo, B. Shi, C. Kuang, W. Xu, S. Cao, Study of scour around submarine pipeline with a rubber plate or rigid spoiler in wave conditions, J. Waterw. Port, Coastal, Ocean Eng. 138 (2012) 484–490.

[10] Y.S. Al Rjoub, J.A. Alshatnawi, Free vibration of functionally-graded porous cracked plates, in: Structures, Elsevier, 2020: pp. 2392–2403.

[11] A. Muc, J. Flis, Flutter characteristics and free vibrations of rectangular functionally graded porous plates, Compos. Struct. 261 (2021) 113301.

[12] Roodgar Saffari P, Fakhraie M, Roudbari MA. Size-Dependent Vibration Problem of Two Vertically-Aligned Single-Walled Boron Nitride Nanotubes Conveying Fluid in Thermal Environment Via Nonlocal Strain Gradient Shell Model. *J Solid Mech*.

[13] Zarabimanesh Y, Roodgar Saffari P, Roudgar Saffari P, et al. Hygro-thermo-mechanical vibration of two vertically aligned single-walled boron nitride nanotubes conveying fluid. *J Vib Control* 2021; 10775463211006512.

[14] Roodgar Saffari P, Fakhraie M, Roudbari MA. Free vibration problem of fluid-conveying double-walled boron nitride nanotubes via nonlocal strain gradient theory in thermal environment. *Mech Based Des Struct Mach* 2020; 1–18.

[15] Roodgar Saffari P, Fakhraie M, Roudbari MA. Free vibration and transient response of heterogeneous piezoelectric sandwich annular plate using third-order shear deformation assumption. Journal of Solid Mechanics. 2020 Jun 30;12(2):315-33.

[16] S. Hashemi, P.K. Shahri, S. Beigzadeh, F. Zamani, M.G. Eratbeni, M. Mahdavi, A. Heidari, H. Khaledi, M.R.R. Abadi, Nonlinear free vibration analysis of In-plane Bi-directional functionally graded plate with porosities resting on elastic foundations, Int. J. Appl. Mech. (2022) 2150131.

[17] T.Q. Quan, N.D. Duc, Analytical solutions for nonlinear vibration of porous functionally graded sandwich plate subjected to blast loading, Thin-Walled Struct. 170 (2022) 108606.

[18] Saffari PR, Fakhraie M, Roudbari MA. Nonlinear vibration of fluid conveying cantilever nanotube resting on visco-pasternak foundation using non-local strain gradient theory. *Micro Nano Lett* 2020; 15: 181–186.

[19] Thongchom C, Refahati N, Roodgar Saffari P, Roudgar Saffari P, Niyaraki MN, Sirimontree S, Keawsawasvong S. An Experimental Study on the Effect of Nanomaterials and Fibers on the Mechanical Properties of Polymer Composites. Buildings. 2022 Jan;12(1):7.

[20] Thongchom C, Jearsiripongkul T, Refahati N, Roudgar Saffari P, Roodgar Saffari P, Sirimontree S, Keawsawasvong S. Sound Transmission Loss of a Honeycomb Sandwich Cylindrical Shell with Functionally Graded Porous Layers. Buildings. 2022 Feb;12(2):151.

[21] Thongchom, C., Saffari, P.R., Refahati, N. et al. An analytical study of sound transmission loss of functionally graded sandwich cylindrical nanoshell integrated with piezoelectric layers. Sci Rep 12, 3048 (2022). https://doi.org/10.1038/s41598-022-06905-1

[22] S. Rebouillat, F. Pla, A Review: On Smart Materials Based on Some Polysaccharides; within the Contextual Bigger Data, Insiders,"Improvisation" and Said Artificial Intelligence Trends, J. Biomater. Nanobiotechnol. 10 (2019) 41–77.

[23] E. Pan, Exact Solution for Simply Supported and Multilayered Magneto-Electro-Elastic Plates, J. Appl. Mech. 68 (2001) 608. https://doi.org/10.1115/1.1380385.

[24] A. Jamalpoor, A. Ahmadi-Savadkoohi, M. Hosseini, S. Hosseini-Hashemi, Free vibration and biaxial buckling analysis of double magneto-electro-elastic nanoplate-systems coupled by a visco-Pasternak medium via nonlocal elasticity theory, Eur. J. Mech. - A/Solids. 63 (2017) 84–98. https://doi.org/10.1016/J.EUROMECHSOL.2016.12.002.

[25] A. Jamalpoor, A. Ahmadi-Savadkoohi, S. Hosseini-Hashemi, Free vibration and biaxial buckling analysis of magneto-electro-elastic microplate resting on visco-Pasternak substrate via modified strain gradient theory, Smart Mater. Struct. 25 (2016) 105035. https://doi.org/10.1088/0964-

1726/25/10/105035.

[26] J.Y. Li, Magnetoelectroelastic multi-inclusion and inhomogeneity problems and their applications in composite materials, Int. J. Eng. Sci. 38 (2000) 1993–2011.

[27] M. Vinyas, S.C. Kattimani, Static analysis of stepped functionally graded magneto-electro-elastic plates in thermal environment: A finite element study, Compos. Struct. 178 (2017) 63–86.

[28] M. Vinyas, Vibration control of skew magneto-electro-elastic plates using active constrained layer damping, Compos. Struct. 208 (2019) 600–617.

[29] M. Vinyas, On frequency response of porous functionally graded magneto-electro-elastic circular and annular plates with different electro-magnetic conditions using HSDT, Compos. Struct. 240 (2020) 112044.

[30] F. Ebrahimi, A. Jafari, M.R. Barati, Vibration analysis of magneto-electro-elastic heterogeneous porous material plates resting on elastic foundations, Thin-Walled Struct. 119 (2017) 33–46.

[31] E. Arshid, A. Kiani, S. Amir, Magneto-electro-elastic vibration of moderately thick FG annular plates subjected to multi physical loads in thermal environment using GDQ method by considering neutral surface, Proc. Inst. Mech. Eng. Part L J. Mater. Des. Appl. 233 (2019) 2140–2159.

[32] M. Hamidi, S. Zaki, M. Aboussaleh, Modeling and numerical simulation of the dynamic behavior of magneto-electro-elastic multilayer plates based on a Winkler-Pasternak elastic foundation, J. Intell. Mater. Syst. Struct. 32 (2021) 832–846.

[33] L.S. Esayas, S. Kattimani, Effect of porosity on active damping of geometrically nonlinear vibrations of a functionally graded magneto-electro-elastic plate, Def. Technol. (2021).

[34] E.L. Sh, S. Kattimani, M. Vinyas, Nonlinear free vibration and transient responses of porous functionally graded magneto-electro-elastic plates, Arch. Civ. Mech. Eng. 22 (2022) 1–26.

[35] N.D. Dat, T.Q. Quan, N.D. Duc, Vibration analysis of auxetic laminated plate with magneto-electro-elastic face sheets subjected to blast loading, Compos. Struct. 280 (2022) 114925.

[36] D.K. Heuer, M.A. Lloyd, D.A. Abrams, G. Baerveldt, D.S. Minckler, M.B. Lee, J.F. Martone, Which is better? One or two?: a randomized clinical trial of single-plate versus double-plate Molteno implantation for glaucomas in aphakia and pseudophakia, Ophthalmology. 99 (1992) 1512–1519.

[37] J.P. Carneal, C.R. Fuller, An analytical and experimental investigation of active structural acoustic control of noise transmission through double panel systems, J. Sound Vib. 272 (2004) 749–771. https://doi.org/10.1016/S0022-460X(03)00418-8.

[38] H. Zhang, D. Shi, S. Zha, Q. Wang, Vibro-acoustic analysis of the thin laminated rectangular plate-cavity coupling system, Compos. Struct. 189 (2018) 570–585.

[39] Y. Qin, Y.-W. Li, X.-Z. Lan, Y.-S. Su, X.-Y. Wang, Y.-D. Wu, Structural behavior of the stiffened double-skin profiled composite walls under compression, Steel Compos. Struct. 31 (2019) 1–12.

[40] P. Oliazadeh, A. Farshidianfar, M.J. Crocker, Study of sound transmission through single-and double-walled plates with absorbing material: Experimental and analytical investigation, Appl. Acoust. 145 (2019) 7–24.

[41] F.X. Xin, T.J. Lu, C.Q. Chen, External mean flow influence on noise transmission through double-leaf aeroelastic plates, AIAA J. 47 (2009) 1939–1951.

[42] F.X. Xin, T.J. Lu, Analytical modeling of sound transmission through clamped triple-panel partition separated by enclosed air cavities, Eur. J. Mech. 30 (2011) 770–782.

[43] R. Talebitooti, V. Johari, M. Zarastvand, Wave transmission across laminated composite plate in the subsonic flow Investigating Two-variable Refined Plate Theory, Lat. Am. J. Solids Struct. 15 (2018).

[44] H. Amirinezhad, A. Tarkashvand, R. Talebitooti, Acoustic wave transmission through a polymeric foam plate using the mathematical model of functionally graded viscoelastic (FGV) material, Thin-Walled Struct. (2020) 106466.

[45] M. Danesh, A. Ghadami, Sound transmission loss of double-wall piezoelectric plate made of functionally graded materials via third-order shear deformation theory, Compos. Struct. (2019).

[46] S.M. Hasheminejad, A. Jamalpoor, Sound transmission control through a hybrid smart double sandwich plate structure, J. Sandw. Struct. Mater. (2020) 1099636220909764.

[47] Q. Mao, Improvement on sound transmission loss through a double-plate structure by using electromagnetic shunt damper, Appl. Acoust. 158 (2020) 107075.

[48] T. Wang, J. Liu, M. Chen, Sound transmission loss of an inertant metamaterial plate submerged in moving fluids, Appl. Math. Model. (2022).

[49] V. Gunasekaran, J. Pitchaimani, L.B.M. Chinnapandi, Acoustic radiation and transmission loss of FG-Graphene composite plate under nonuniform edge loading, Eur. J. Mech. 88 (2021) 104249.

[50] M. Ghassabi, R. Talebitooti, Acoustic insulation feature of multiphase magneto-electro-elasticity shell systems with double curvature, Mech. Adv. Mater. Struct. (2021) 1–13.

[51] M. Hosseini, M.R. Mofidi, A. Jamalpoor, M.S. Jahanshahi, Nanoscale mass nanosensor based on the vibration analysis of embedded magneto-electro-elastic nanoplate made of FGMs via nonlocal Mindlin plate theory, Microsyst. Technol. 24 (2018) 2295–2316.

[52] S.I. Tahir, A. Tounsi, A. Chikh, M.A. Al-Osta, S.U. Al-Dulaijan, M.M. Al-Zahrani, An integral four-variable hyperbolic HSDT for the wave propagation investigation of a ceramic-metal FGM plate with various porosity distributions resting on a viscoelastic foundation, Waves in Random and Complex Media. (2021) 1–24.

[53] Y.S. Li, Buckling analysis of magnetoelectroelastic plate resting on Pasternak elastic foundation, Mech. Res. Commun. 56 (2014) 104–114. https://doi.org/10.1016/j.mechrescom.2013.12.007.

[54] M. Arefi, M. Kiani, M.H. Zamani, Nonlocal strain gradient theory for the magneto-electro-elastic vibration response of a porous FG-core sandwich nanoplate with piezomagnetic face sheets resting on an elastic foundation, J. Sandw. Struct. Mater. 22 (2020) 2157–2185.

[55] T. Lu, F. Xin, Vibro-acoustics of lightweight sandwich structures, Springer, 2014.

[56] A. Shooshtari, S. Razavi, Vibration analysis of a magnetoelectroelastic rectangular plate based on a higher-order shear deformation theory, Lat. Am. J. Solids Struct. 13 (2016) 554–572.

[57] S. Soni, N.K. Jain, P. V Joshi, Analytical modeling for nonlinear vibration analysis of partially

cracked thin magneto-electro-elastic plate coupled with fluid, Nonlinear Dyn. 90 (2017) 137–170.

[58] L. Hadji, M. Avcar, Ö. Civalek, An analytical solution for the free vibration of FG nanoplates, J. Brazilian Soc. Mech. Sci. Eng. 43 (2021) 1–14.

[59] F.X. Xin, T.J. Lu, Analytical and experimental investigation on transmission loss of clamped double panels: Implication of boundary effects, J. Acoust. Soc. Am. 125 (2009) 1506–1517. https://doi.org/10.1121/1.3075766.

Table 1. Material properties of the MEE-PFGM plate and acoustic medium.

Properties (MEE Layer)	$BaTiO_3 - CoFe_2O_4$
Elastic (GPa)	$c_{11} = 226, c_{12} = 125, c_{22} = 226,$ $c_{44} = 44.2, c_{55} = 44.2, c_{66} = 51$
Piezoelectric ($C\ m^{-2}$)	$e_{31} = -2.2, e_{32} = -2.2,$ $e_{24} = 5.8, e_{15} = 5.8$
Dielectric ($10^{-9} C\ V^{-1}\ m^{-1}$)	$\kappa_{11} = 5.64,\quad \kappa_{22} = 5.64,$ $\kappa_{33} = 6.35$
Piezomagnetic ($N\ A^{-1}\ m^{-1}$)	$f_{31} = 290.1, e_{32} = 290.1,$ $e_{24} = 275, e_{15} = 275$
Magnetoelectric ($10^{-12} N\ S\ V^{-1}\ C^{-1}$)	$\mu_{11} = 5.367, \mu_{11} = 5.367,$ $\mu_{33} = 2737.5$
Magnetic ($10^{-6} N\ s^2\ C^{-2}$)	$\gamma_{11} = -297,\quad \gamma_{22} = -297,$ $\gamma_{33} = 83.5$
Mass density ($Kg\ m^{-3}$)	$\rho_m = 5550$

Properties (FGM Core)	**Si3N4 (ceramic)**	**SUS304 (metal)**
Elastic (GPa)	$E = 348.43$	$E = 201.4$
Poisson's Ratio	$\vartheta = 0.3$	$\vartheta = 0.3$
Mass density (Kg m^{-3})	$\rho = 2370$	$\rho = 8166$
Properties (Acoustic medium)	Air	
Sound Speed (m s^{-1})	$c_0 = 343$	
Mass density (Kg m^{-3})	$\rho_0 = 1.21$	

Table 2. Comparison of dimensionless natural frequency of a MEE plate.

Aspect Ratio (a/b)	Present (FSDA)	Ref. [56] (HSDT)	Ref. [57] (CPT)
0.5	0.342	0.343	0.366
1	0.531	0.535	0.585
2	1.236	1.233	1.463

Table 3. Comparison of dimensionless natural frequency of a FGM plate.

p	Study	ω_1	ω_2	ω_3
0	present	0.092	0.221	0.338
	Ref. [50]	0.093	0.222	0.341
2	present	0.049	0.116	0.177
	Ref. [50]	0.049	0.116	0.178

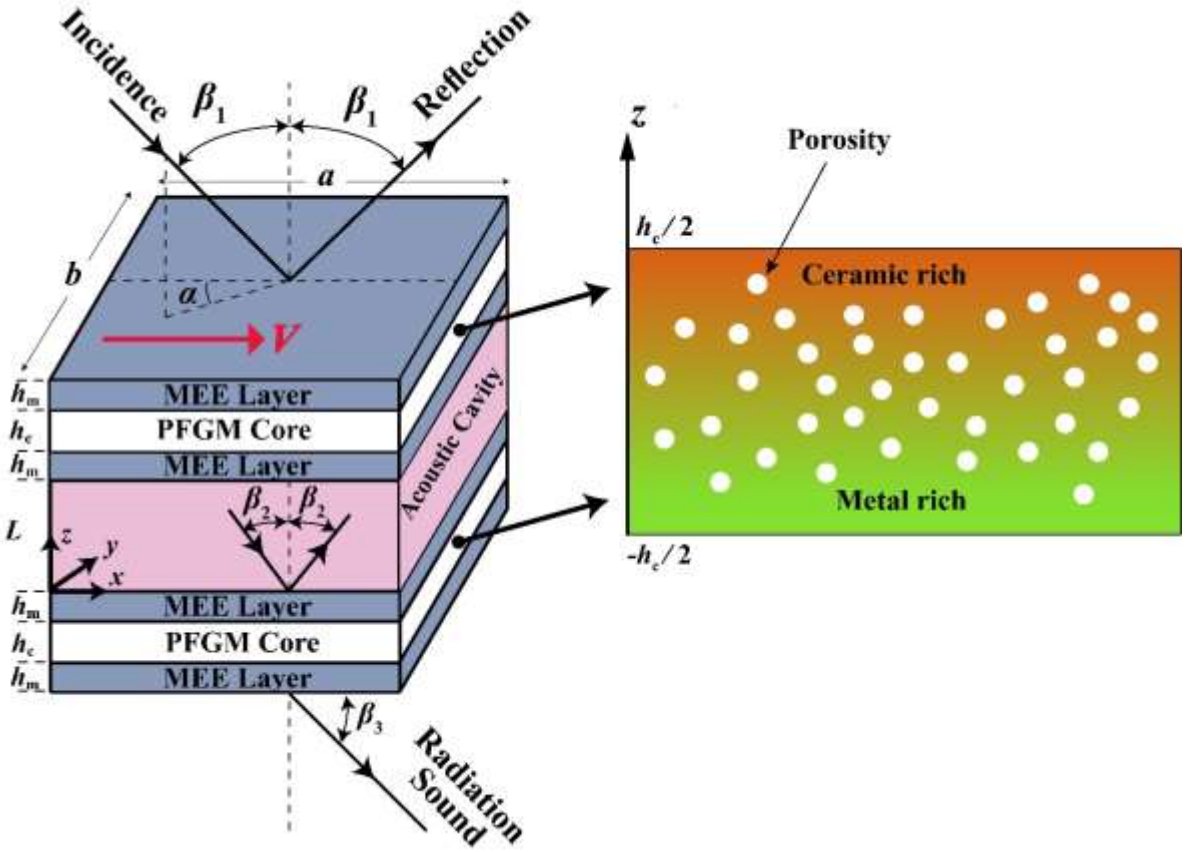

Fig. 1. The schematic of double-walled MEE-PFGM plate under incidence wave and external mean airflow.

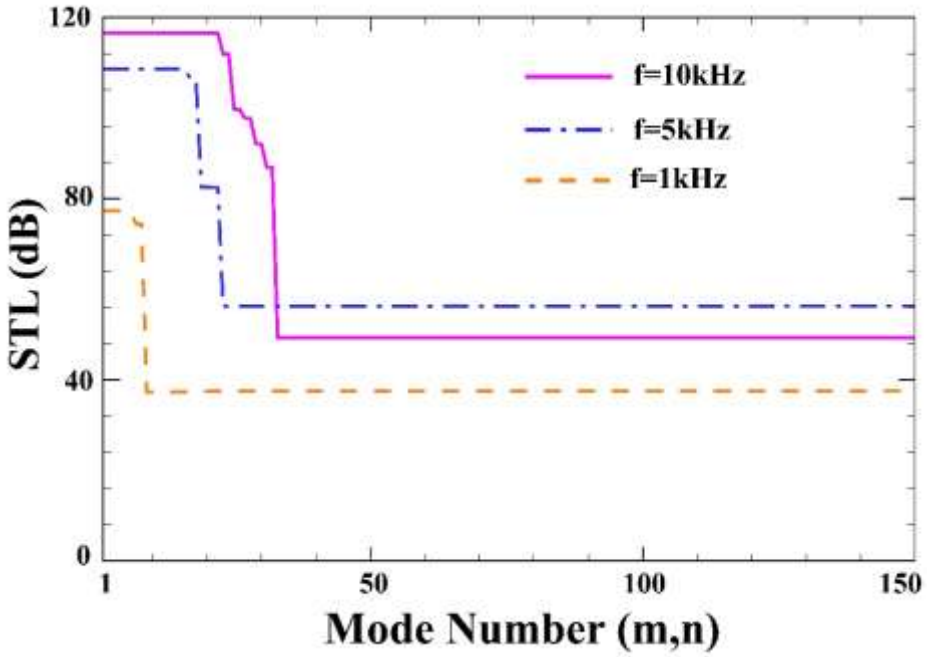

Fig. 2. Mode convergence diagram for double-walled MEE-PFGM plate.

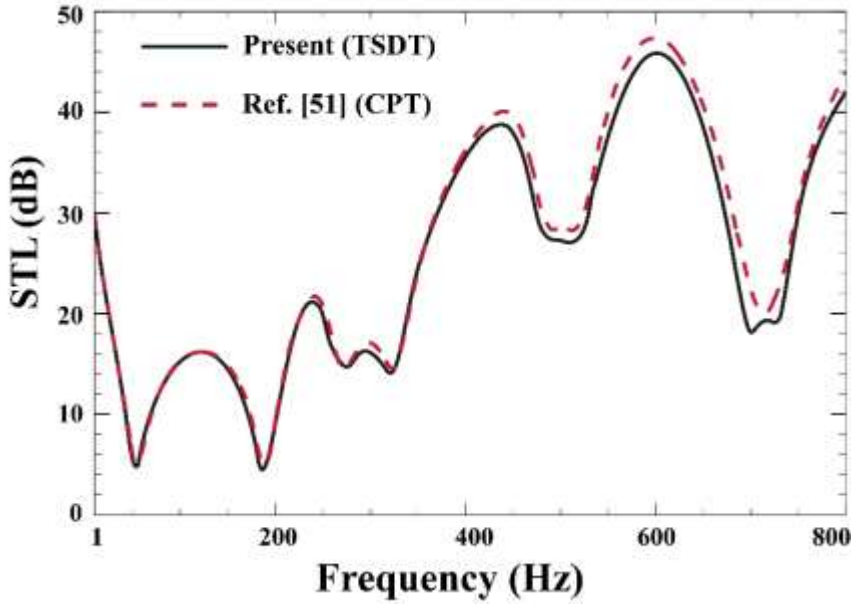

Fig. 3. Comparison study of STL curves for double-walled elastic plate.

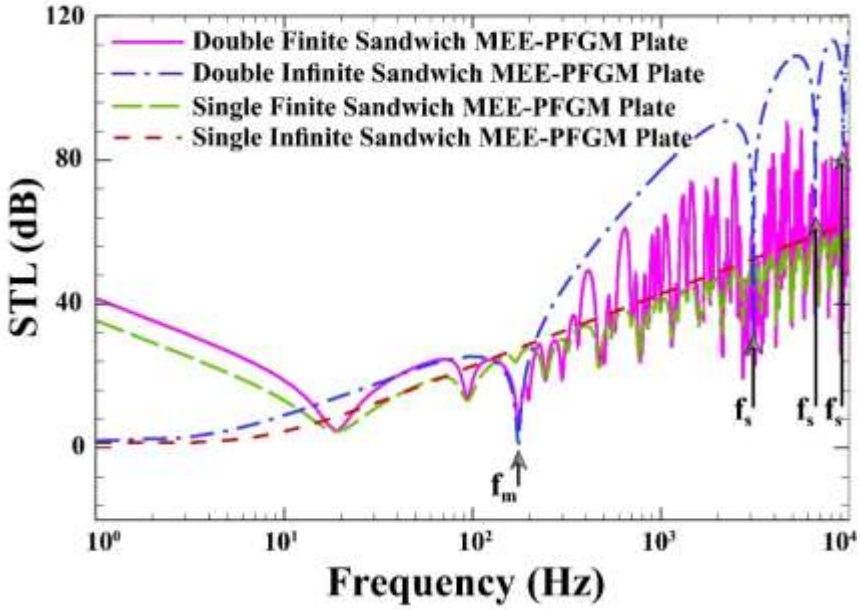

Fig. 4. The variations of STL through single/double-walled MEE-PFGM plate versus plate dimensions.

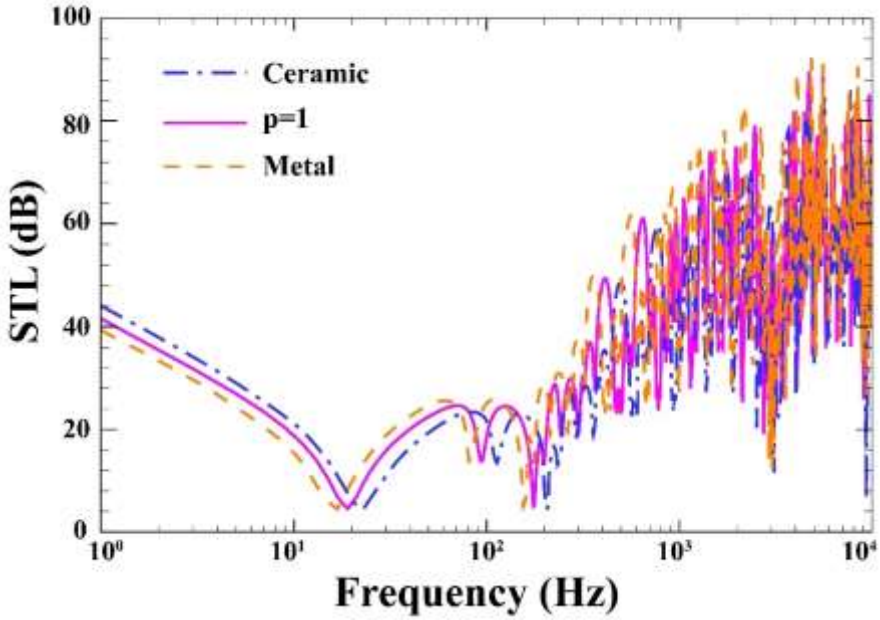

Fig. 5. Effect of the material gradient index on the STL through double-walled MEE-PFGM plate.

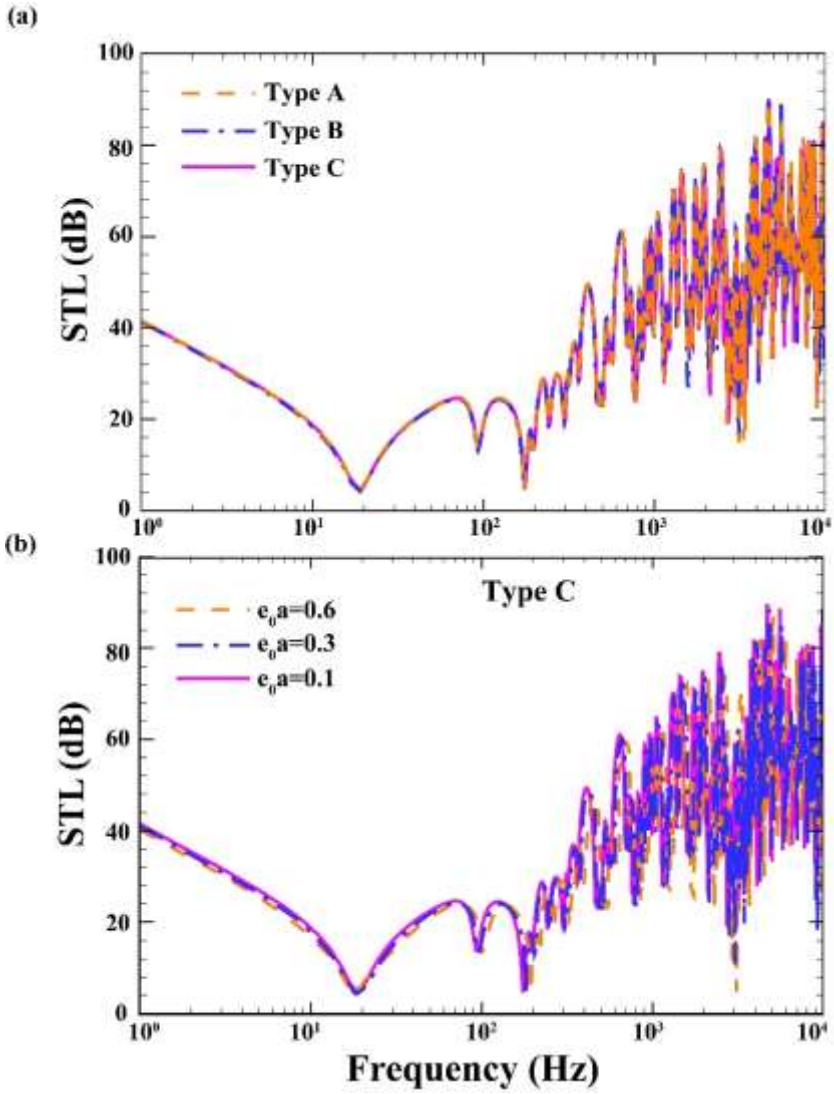

Fig. 6. The STL of double-walled MEE-PFGM plate (a): against the porosity distribution models; (b) against the porosity coefficient.

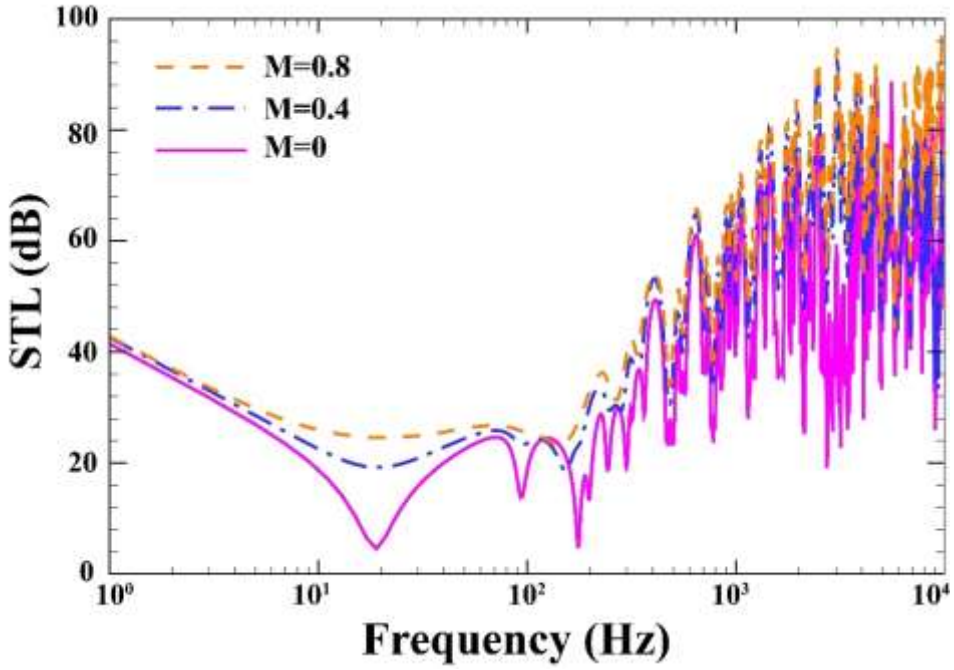

Fig. 7. The effect of the external flow Mach number on the STL of double-walled MEE-PFGM plate.

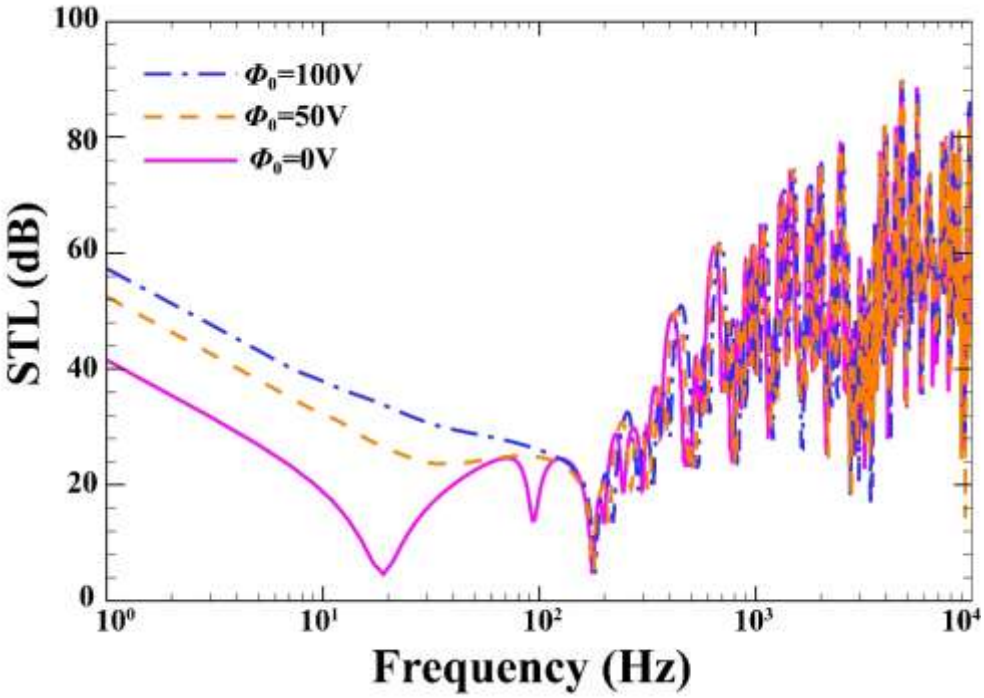

Fig. 8. The effect of the external electric potential on the changes of STL through double-walled MEE-PFGM plate.

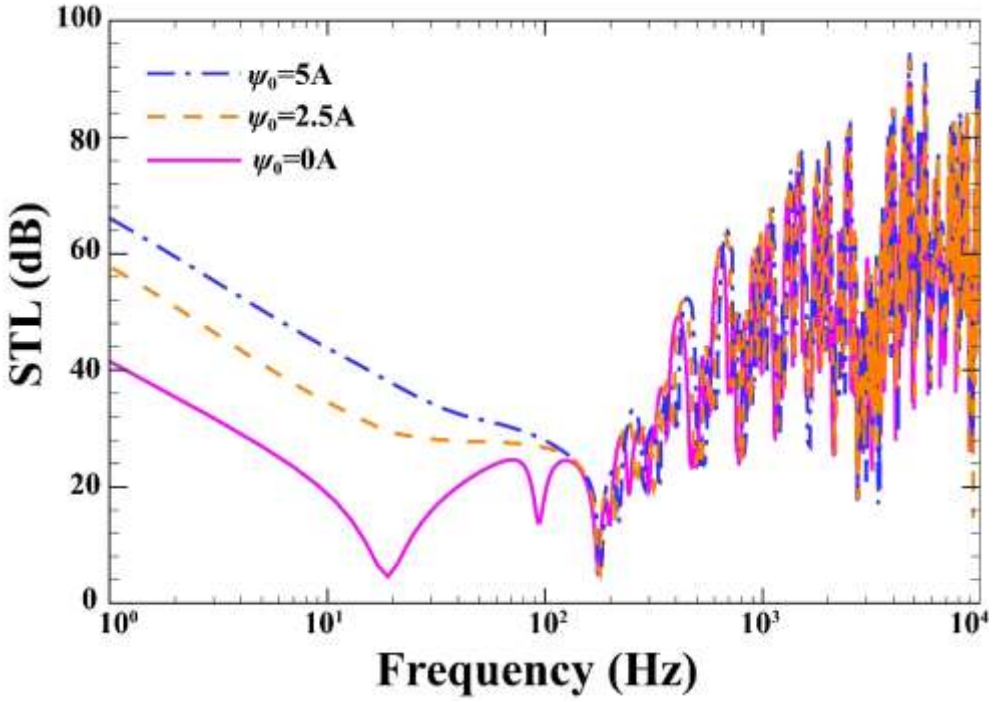

Fig. 9. The effect of the external magnetic potential on the changes of STL through double-walled MEE-PFGM plate.

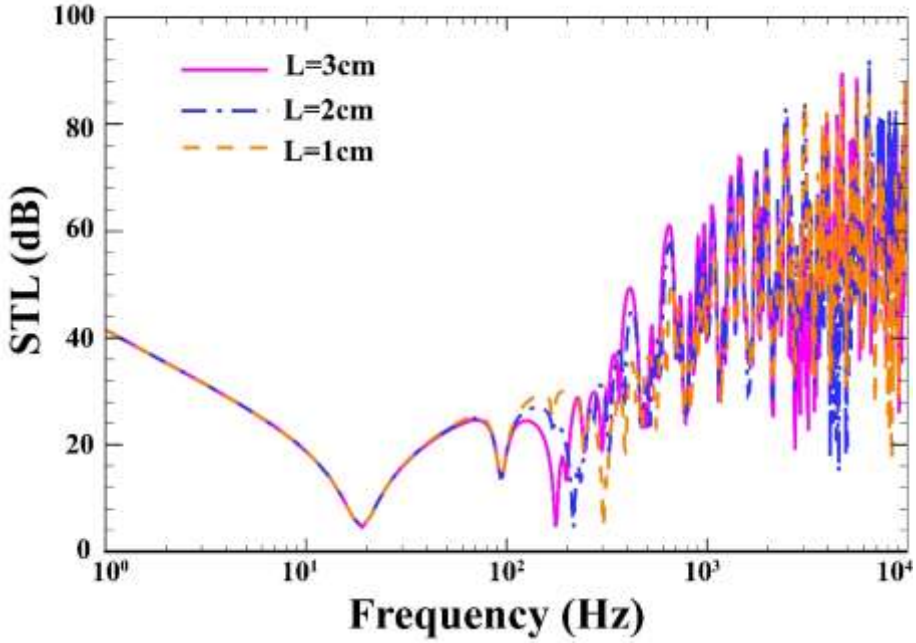

Fig. 10. The effect of the air cavity depth on STL curves of double-walled MEE-PFGM plate.

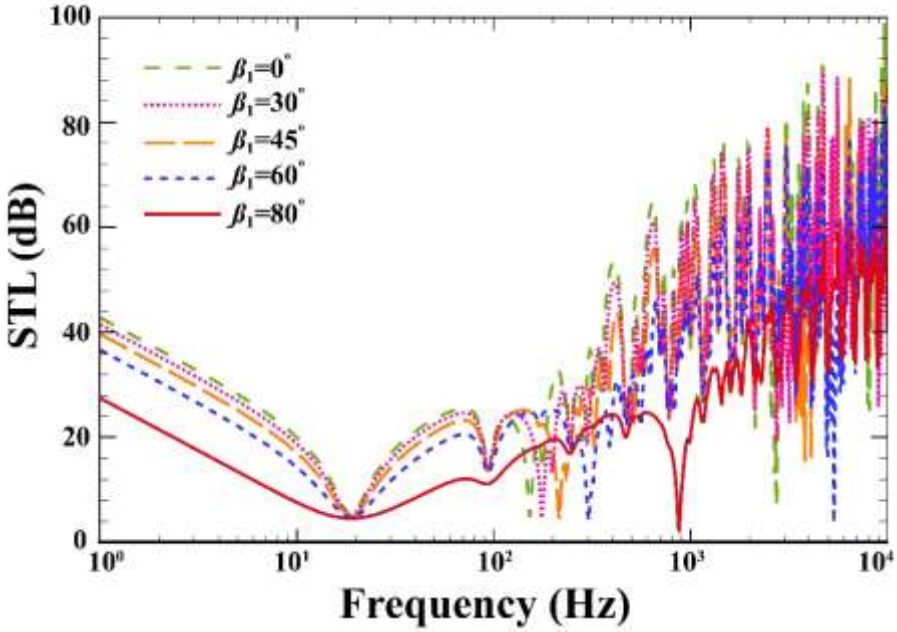

Fig. 11. The effect of elevation angle on STL curves of double-walled MEE-PFGM plate.

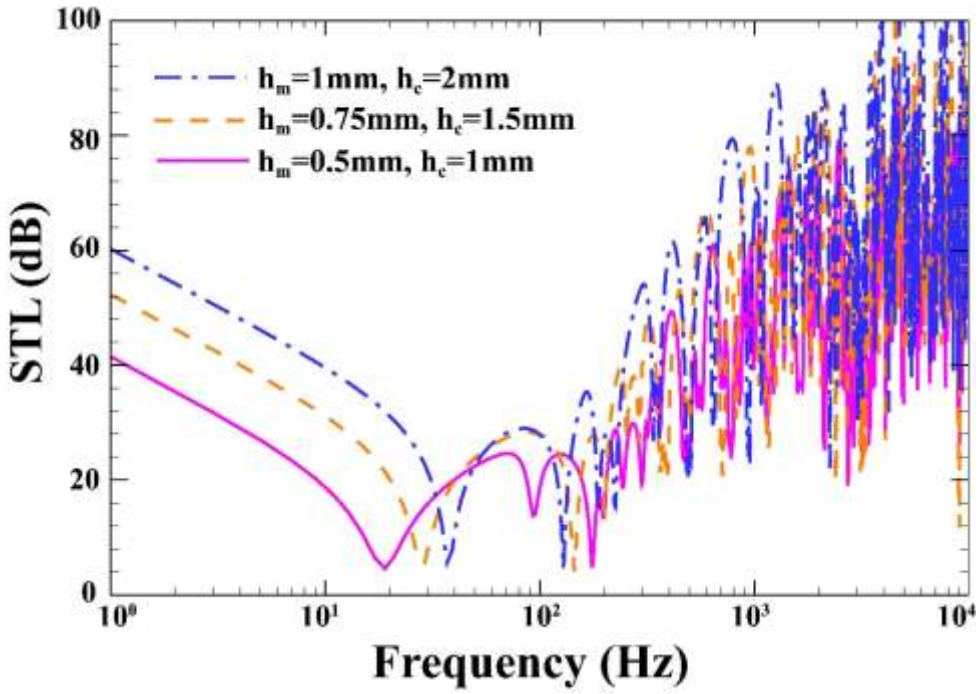

Fig. 12. The effect of sandwich MEE-PFGM plate thickness on the variations of STL

Supplementary Files

This is a list of supplementary files associated with this preprint. Click to download.

- AppendixSupplementary.docx